

RESEARCH

Open Access



# Cocaine regulates antiretroviral therapy CNS access through pregnane-x receptor-mediated drug transporter and metabolizing enzyme modulation at the blood brain barrier

Rodnie Colón Ortiz<sup>1†</sup>, Stephen Knerler<sup>2†</sup>, Lisa B. Fridman<sup>2</sup>, Alicia Mercado<sup>2</sup>, Amira-Storm Price<sup>2</sup>, Jose J. Rosado-Franco<sup>2</sup>, Hannah Wilkins<sup>3</sup>, Bianca R. Flores<sup>2</sup>, Benjamin C. Orsburn<sup>3</sup> and Dionna W. Williams<sup>1,2,3,4,5,6\*</sup>

## Abstract

**Background** Appropriate interactions between antiretroviral therapies (ART) and drug transporters and metabolizing enzymes at the blood brain barrier (BBB) are critical to ensure adequate dosing of the brain to achieve HIV suppression. These proteins are modulated by demographic and lifestyle factors, including substance use. While understudied, illicit substances share drug transport and metabolism pathways with ART, increasing the potential for adverse drug:drug interactions. This is particularly important when considering the brain as it is relatively under-treated compared to peripheral organs and is vulnerable to substance use-mediated damage.

**Methods** We used an in vitro model of the human BBB to determine the extravasation of three first-line ART drugs, emtricitabine (FTC), tenofovir (TFV), and dolutegravir (DTG), in the presence and absence of cocaine, which served as our illicit substance model. The impact of cocaine on BBB integrity and permeability, drug transporters, metabolizing enzymes, and their master transcriptional regulators were evaluated to determine the mechanisms by which substance use impacted ART central nervous system (CNS) availability.

**Results** We determined that cocaine had a selective impact on ART extravasation, where it increased FTC's ability to cross the BBB while decreasing TFV. DTG concentrations that passed the BBB were below quantifiable limits. Interestingly, the potent neuroinflammatory modulator, lipopolysaccharide, had no effect on ART transport, suggesting a specificity for cocaine. Unexpectedly, cocaine did not breach the BBB, as permeability to albumin and 4 kDa FITC-dextran, as well as tight junction proteins and adhesion molecules remained unchanged. Rather, cocaine selectively decreased the pregnane-x receptor (PXR), but not constitutive androstane receptor (CAR). Consequently, drug transporter expression and activity decreased in endothelial cells of the BBB, including p-glycoprotein (P-gp), breast cancer resistance protein (BCRP), and multidrug resistance-associated protein 4 (MRP4). Further, cytochrome P450 3A4 (CYP3A4) enzymatic activity increased following cocaine treatment that coincided with decreased expression. Finally, cocaine modulated adenylate kinases that are required to facilitate biotransformation of ART prodrugs to their phosphorylated, pharmacologically active counterparts.

<sup>†</sup>Rodnie Colón Ortiz and Stephen Knerler contributed equally.

\*Correspondence:

Dionna W. Williams  
dwill4@emory.edu

Full list of author information is available at the end of the article



© The Author(s) 2024. **Open Access** This article is licensed under a Creative Commons Attribution 4.0 International License, which permits use, sharing, adaptation, distribution and reproduction in any medium or format, as long as you give appropriate credit to the original author(s) and the source, provide a link to the Creative Commons licence, and indicate if changes were made. The images or other third party material in this article are included in the article's Creative Commons licence, unless indicated otherwise in a credit line to the material. If material is not included in the article's Creative Commons licence and your intended use is not permitted by statutory regulation or exceeds the permitted use, you will need to obtain permission directly from the copyright holder. To view a copy of this licence, visit <http://creativecommons.org/licenses/by/4.0/>. The Creative Commons Public Domain Dedication waiver (<http://creativecommons.org/publicdomain/zero/1.0/>) applies to the data made available in this article, unless otherwise stated in a credit line to the data.

**Conclusion** Our findings indicate that additional considerations are needed in CNS HIV treatment strategies for people who use cocaine, as it may limit ART efficacy through regulation of drug transport and metabolizing pathways at the BBB.

**Keywords** Blood brain barrier, Antiretroviral therapy, HIV, Cocaine, Drug transport, Drug metabolism, Pregnane-X receptor

## Background

The current treatment strategy for the human immunodeficiency virus-1 (HIV) includes the use of antiretroviral therapies (ART) that target distinct steps of the viral life cycle, including entry, reverse transcription, and integration. ART administration occurs in a combinatorial fashion wherein two to three drugs from differing classes, termed combined ART (cART), are co-administered to facilitate suppressed viral replication. As a result, cART has revolutionized the HIV epidemic by decreasing the rates of opportunistic infections, acquired immunodeficiency syndrome (AIDS), HIV-related morbidity and mortality, and HIV transmission while increasing the lifespan for people living with the virus [1–4]. However, treating HIV in tissues, including the brain, remains a challenge due to the limited potential of ART to bypass tissue barriers like the blood brain barrier (BBB) [5–11]. This limited tissue access prevents organs from receiving adequate ART concentrations necessary for complete viral suppression and results in the development of sanctuaries that remain a major barrier to HIV eradication efforts [12, 13]. Thus, it is imperative to understand more completely the mechanisms that impact ART access to the brain and other tissue sanctuaries.

It is not surprising that ART has difficulty traversing the BBB, as ~98% of all small molecule therapeutic drugs face this same obstacle [14, 15]. ART disposition in the brain requires navigating a complex and nuanced interplay between transporter proteins and drug metabolizing enzymes [16]. Membrane-associated drug transporters facilitate influx into and efflux out of the CNS and primarily belong to ATP-binding cassette (ABC) and solute carrier (SLC) transporter superfamilies. While small, lipophilic, and uncharged molecules can passively diffuse through the BBB, large, hydrophobic, and charged molecules require facilitated and/or active transport by ABC and SLC transporters. A non-exhaustive list of the ABC and SLC transporters known to interact with ART include: P-glycoprotein (P-gp), multidrug resistance-associated protein 1 (MRP1), multidrug resistance-associated protein 2 (MRP2), multidrug resistance-associated protein 4 (MRP4), breast cancer resistance protein (BCRP), equilibrative nucleoside transporter (ENT1), organic anion transporter 1 (OAT1), organic anion transporter 3 (OAT3), and organic anion-transporting polypeptide

1A2 (OATP1A2) [17–19]. Drug metabolism is another obstacle that must be faced at the BBB, as phase I and II enzymes facilitate biotransformation through the addition of moieties (including oxygen and glucuronide groups) that increase hydrophilicity and aid in excretion. Of these, cytochrome P450 (CYP) 3A4 (CYP3A4) is among the most notable as it interacts with multiple ART classes, including reverse transcriptase inhibitors, protease inhibitors, entry inhibitors, and integrase inhibitors [20–22]. Biotransformation is another aspect of drug metabolism particularly relevant for the ART's administered as prodrugs, as it involves the addition of molecules to the parent drug required for becoming pharmacologically active. Adenylate kinases (AK) are one example of this, which, through their phosphorylation activity, facilitate the antiviral capacity of ART [23–25].

Drug transport and metabolism mechanisms are complex and encompass an interconnected web where simultaneous competing mechanisms occur due to wide and overlapping substrate specificity. For example, the reverse transcriptase inhibitor tenofovir (TFV) is the substrate of BCRP, MRP2, MRP4, OAT1, OAT3, and ENT1 while it can also induce P-gp, MRP1, MRP2, and MRP3 [18, 19]. While not a substrate of CYP3A4, TFV can inhibit other CYP isoforms and requires kinase-mediated phosphorylation to become pharmacologically active [24, 26–30]. It is also important to consider the intertwined nature of drug transport and metabolism mechanisms during HIV due to the combinatorial nature of cART. The co-administration of multiple drugs with overlapping specificity for drug transporters and metabolizing enzymes requires the interplay of multiple pathways to maintain appropriate ART concentrations and therapeutic efficacy. ART is not the only factor that must be taken into consideration, particularly as it pertains to treating sanctuary sites. One must consider the person behind the disease and the unique factors in their lives that may impact the ability of ART to work effectively, including diet, age, sex, and racial and/or ethnic background [31–37]. For example, polypharmacy is highly prevalent in people living with HIV as many individuals also receive treatment for comorbid diseases [38]. This creates the opportunity for drug:drug interactions that may change the pharmacologic profile of ART.

Substance use is another important, yet understudied, factor when evaluating ART access to the brain. Substance use is inextricably linked with the HIV epidemic and increases the risk of HIV acquisition [39–42]. Further, the rate of substance use is higher among people living with HIV compared to seronegative individuals [43–47]. Of importance, substance use is associated with poorer HIV outcomes, which is often attributed to decreased ART adherence [48–52]. However, it is unlikely that every person with HIV who consumes illicit substances discontinues taking ART as prescribed. While this may certainly occur for some individuals, the molecular consequences of substance use on ART efficacy should also be considered. Interestingly, adverse drug:drug reactions exist between substances of abuse and ART, due to shared drug transport and metabolism pathways, which can lead to decreased ART efficacy, increased toxicity, and poorer outcomes for people living with HIV [53–59]. Additionally, the impact of substance use on ART efficacy in the brain is of particular importance, as illicit substances are well known to impact BBB and CNS function [60–67].

Extensive regulatory mechanisms exist to ensure the proteins involved in drug transport and metabolism fulfill their endogenous responsibilities, while also promoting detoxification of the cell and xenobiotic clearance. Two players are tasked with being the master orchestrators of these pathways: the nuclear receptors pregnane-X receptor (PXR) and constitutive androstane receptor (CAR) [68]. These ligand-activated transcription factors are xenobiotic sensors that, following activation, coordinately regulate genes encoding drug transporters and drug metabolizing proteins [69–71]. They have overlapping activity and interact widely with licit and illicit pharmacologically active substances [72–74]. PXR and CAR are highly expressed at the BBB where they regulate the activity of drug transporter and metabolizing enzymes, including P-gp, BCRP, and MRP2 [75–82]. Additionally, their downregulation can decrease the expression and activity of drug transporters. Of importance, ART and substances of abuse are capable of inducing changes in drug transporter and metabolizing enzyme expression through interactions with PXR and CAR, which may alter their anti-HIV pharmacokinetic properties [18, 19, 83, 84]. Moreover, the modulation of PXR and CAR may promote adverse drug:drug interactions between substances of abuse and ART that can result in decreased antiviral efficacy and potentially treatment failure – especially in the brain and other tissue reservoirs.

We used cocaine as a model illicit substance to evaluate the impact of substance use on ART CNS availability through interactions at the BBB. Our study centered on three ART drugs that represent a first-line HIV regimen:

emtricitabine (FTC), TFV, and dolutegravir (DTG). Using a transwell model of the human BBB, we evaluated the ability of FTC, TFV, and DTG to cross from the apical to basolateral chamber in the presence and absence of cocaine, or lipopolysaccharide (LPS) as a control. We identified an inherent differential capacity of ART to cross the BBB, where TFV had the highest extravasation rate followed by FTC. DTG's extravasation across the BBB was below quantifiable limits. Cocaine, but not LPS, altered ART's ability to cross the BBB where it increased FTC, but decreased TFV. Unexpectedly, cocaine's effects on ART extravasation did not cause BBB disruption. Instead, cocaine decreased PXR that resulted in altered drug transporter and drug metabolizing enzyme expression and activity. Of note, cocaine's effects were specific to PXR as CAR remained unchanged. Our findings demonstrate that cocaine can regulate ART bioavailability and efficacy in the CNS by regulating drug transport and metabolism activity at the BBB. Further, our study suggests substance use must be taken into consideration in ART prescription recommendations to ensure all people with HIV have an equal chance to achieve viral suppression, especially in sanctuaries like the brain.

## Methods

### Cells

Primary human astrocytes (ScienCell Research Laboratories, Carlsbad, CA) were grown to confluence in Basal Medium Eagle (Thermo Fisher Scientific, Waltham, MA) buffered to pH ranging from 7.2–7.5 with 2.2 g/L sodium bicarbonate and 15 mM HEPES (Gibco, Grand Island, New York). Media was supplemented with 2% fetal bovine serum (FBS) (R&D Systems, Minneapolis, MN), 1% penicillin–streptomycin 10,000U/mL (Gibco), and 1% astrocyte growth supplement (ScienCell Research Laboratories). Astrocytes were used at passages 3–4 for all experiments.

Primary human brain microvascular endothelial cells (Cell Systems, Kirkland, WA) were grown to confluence on tissue culture plates coated with 0.2% gelatin (Thermo Fisher Scientific) in medium 199 (M199) (Gibco) buffered to pH ranging from 7.2–7.5 with 2.2 g/L sodium bicarbonate and 15 mM HEPES (Gibco). Complete M199 media (M199C) was comprised of 20% heat-inactivated newborn calf serum (Gibco), 1% penicillin–streptomycin 10,000U/mL (Gibco), 25 mg/L heparin (Sigma, St. Louis, MO), 5% heat-inactivated human serum AB (GeminBio, Sacramento, CA), 50 mg/L ascorbic acid (Sigma), 7.5 mg/L endothelial cell growth supplement (Sigma), 2 mM L-glutamine (Gibco), and 5 mg/L bovine brain extract (Lonza, San Diego, CA). Endothelial cells were used at passages 9–16 for all experiments.

### **In vitro Model of the Human BBB**

Our in vitro transwell model of the human BBB model was made as previously described [85–91]. Briefly, astrocytes ( $1 \times 10^5$  cells/insert) were seeded on the underside of a tissue culture insert comprised of a polycarbonate membrane with 3  $\mu$ M pores (Falcon, Corning, NY) and allowed to adhere for four hours at 37 °C, 5% CO<sub>2</sub> while continually being fed in 5–30 min intervals with M199C. The tissue culture inserts were then inverted and transferred to a 24-well tissue culture plate (Falcon) containing M199C. Endothelial cells ( $4 \times 10^4$  cells/insert) were seeded into the upperside of the insert that was pre-coated with 0.2% gelatin (Thermo Fisher Scientific). The cells grew to confluence at 37 °C, 5% CO<sub>2</sub> over three days, during which time the astrocyte processes penetrated through the pores to establish contact with the endothelial cells and seal the barrier. The BBB model was used for experiments following four days of culture.

### **Evans Blue Albumin Permeability Assay**

Permeability of our in vitro BBB model was first evaluated using Evans Blue dye conjugated to albumin (EBA). To prepare the EBA dye, 0.45% Evans Blue (Sigma) was conjugated to bovine serum albumin (Thermo Fisher Scientific) by incubation at 37 °C overnight while rotating continuously. Excess unbound dye was removed by ice cold ethanol washes that consisted of precipitation with 100% molecular grade ethanol (The Warner Graham Company, Cockeysville, MD) at -80 °C for 30 min, centrifugation at 4 °C at maximum speed (21,130 g) for 10 min, removal of the unbound dye-containing supernatant, mechanical dissociation of the albumin pellet, and washing with ice cold ethanol prior to repeating albumin precipitation at -80 °C. The ethanol precipitation and washes were repeated for ~40 cycles until the supernatants were clear and all unbound Evans Blue dye was removed.

BBB permeability was determined by adding EBA to the apical portion of our transwell model for 30 min at 37 °C, 5% CO<sub>2</sub> and allowing it to pass into the basolateral chamber containing phenol red free Dulbecco's Modified Eagle Medium (Gibco). After the indicated time, the media contained in the basolateral portion was collected and the absorbance spectrophotometrically evaluated at 620 nm. EBA dye added to phenol red free Dulbecco's Modified Eagle Medium served as a positive control to determine quantitation of the absorbance value corresponding to a complete breach of the BBB.

### **Fluorescein (FITC) dextran permeability assay**

Permeability of our in vitro BBB model was further evaluated by a complimentary method using 4 kDa

FITC-Dextran (Sigma). A 1 mg/mL FITC-Dextran stock was added to the apical portion of our transwell model for 30 min at 37 °C, 5% CO<sub>2</sub> and allowed to pass into the basolateral chamber containing phenol red free Dulbecco's Modified Eagle Medium. After the indicated time, the media contained in the basolateral portion was collected and the fluorescence measured with the Spectra Max iD5 (Molecular Devices, San Jose, CA) microplate reader at an excitation and emission wavelength of 490/520 nm. FITC-Dextran added to phenol red free Dulbecco's Modified Eagle Medium served as a positive control to determine quantitation of the fluorescence value corresponding to a complete breach of the BBB.

### **ART BBB Extravasation assay**

FTC, TFV, and DTG (all from Toronto Research Chemicals, Toronto, Canada) were reconstituted to 10  $\mu$ M in M199C and added the apical portion of the BBB model in the presence or absence of 10 ng/mL LPS (Sigma) or 10  $\mu$ M cocaine hydrochloride (NIDA Drug Supply Program, Research Triangle Park, NC) for 24 h at 37 °C, 5% CO<sub>2</sub>. M199C alone was used as a negative control. After the indicated time, the media contained in the basolateral portion was collected, aliquoted, and stored at -80 °C until quantitation by tandem liquid chromatography-mass spectrometry analyses. There were no freeze/thaw cycles before quantitation.

### **ART Concentration determination**

The concentrations of FTC, TFV, and DTG that passed through the BBB model were determined using validated liquid chromatographic-mass spectrometric methods by the Clinical Pharmacology Analytic Laboratory at the Johns Hopkins University School of Medicine, as previously described [92, 93]. Briefly, FTC and TFV were analyzed in positive mode using a TSQ Vantage<sup>®</sup> triple quadrupole mass spectrometer coupled with a HESI II<sup>®</sup> probe (Thermo Scientific). The analytical run time was 8 min, and the assay lower limits of quantitation were 5 and 1 ng/mL for FTC and TFV, respectively. DTG was analyzed using an API 5000 mass analyzer (SCIEX, Redwood City, CA, USA) interfaced with a Waters Acquity UPLC system (Waters Corporation, Milford, MA, USA). The analytical run time was 2–5 min, and the assay lower limit of quantitation was 100 ng/mL. DTG concentrations below 100 ng/mL were reported as below the limit of quantitation. Assays were validated in accordance with the FDA Guidance for Industry, Bioanalytical Method Validation recommendations and by the Clinical Pharmacology Quality Assurance program [94, 95]. All performance parameters were acceptable. Each experimental replicate for all ART quantification findings includes data collected from seven independent BBB models, where

five independent measures of the supernatant were evaluated from five distinct supernatant aliquots.

#### **LEGENDPlex multiplex bead-based cytokine analysis**

Cytokine production, indicative of activation of the innate immune response, was determined using the Biolegend LEGENDPlex platform (San Diego, CA) through flow cytometric analyses. The apical portion of our BBB model was treated with 10  $\mu$ M cocaine, 100 ng/mL LPS, or vehicle for 24 h, after which time supernatant from the apical portion was collected, aliquoted, and stored at -80 °C until cytokine determination was performed. Importantly, there were no freeze/thaw cycles of the supernatant prior to analysis. The LegendPlex bead-based immunoassay was performed following the manufacturer's protocol and concentrations were determined using 7 parameter log curve fits with vendor provided standards and quality controls. The Human Anti-Virus Response Panel was used to measure IL-1 $\beta$ , IL-6, TNF- $\alpha$ , IP-10, IFN- $\lambda$ 1, IL-8, IL-12p70, IFN- $\alpha$ 2, IFN- $\lambda$ 2/3, GM-CSF, IFN- $\beta$ , IL-10, and IFN- $\gamma$ .

#### **Endothelial cell cocaine treatment**

When 80% confluent, primary human endothelial cells were treated with 0.01–100  $\mu$ M cocaine hydrochloride for 24 h, after which time they were used in all subsequent downstream assays. Ten  $\mu$ M was the primary concentration of cocaine used throughout the study as we did not determine a dose-specific response (Fig. 6E). Further, 10  $\mu$ M is consistent with the  $8.6 \pm 1.6$   $\mu$ M range that occurs clinically [96]. Treatment with vehicle was used as a control.

#### **Endothelial cell norcocaine and benzoylecgonine treatment**

When 80% confluent, primary human endothelial cells were treated with 0.01–100  $\mu$ M norcocaine or benzoylecgonine (both from Research Triangle Institute, Research Triangle Park, NC) for 24 h, after which time they were used in all subsequent downstream assays. Ten  $\mu$ M was the primary concentration of each cocaine metabolite used throughout the study as the metabolites did not have an effect on PXR (Fig. 6F), which we determined occurred irrespective of concentration (data not shown). Further, 10  $\mu$ M is consistent with the  $9.2 \pm 5.2$   $\mu$ M and  $4.4 \pm 4.4$   $\mu$ M range that occurs clinically [96]. Treatment with vehicle was used as a control.

#### **Cell viability determination**

Endothelial cells were treated with cocaine hydrochloride (10  $\mu$ M) for 0.5 and 24 h, after which time viability was assessed using the BD Horizon Fixable Viability Stain 520 (BD), according to manufacturer's instructions.

#### **Quantitative RT-PCR**

Endothelial cells were lysed with Buffer RLT Plus (Qiagen, Germantown, MD) supplemented with 1%  $\beta$ -mercaptoethanol (Sigma). Total RNA was isolated using the RNeasy Mini Kit (Qiagen) according to the manufacturer's protocol with the modification of on column DNase digestion using RQ1 RNase free DNase (Promega, Madison, WI) in the enzyme mix. Complementary DNA (cDNA) synthesis was performed using 1  $\mu$ g of total RNA with the iScript cDNA Synthesis Kit (Bio-Rad, Hercules, CA). The gene encoding for the zonula occludens-1 (Zo-1, catalogue Hs01551861\_m1 TJP1) and 18S (catalogue Hs03003631\_g1 18S FAM) proteins were evaluated by qRT-PCR using a TaqMan Gene Expression Assay (Thermo Fisher Scientific, Waltham, MA) using the Bio-Rad CFX96 Real-Time System with cycling conditions optimized for the TaqMan Fast Advanced Master Mix (enzyme activation at 95 °C for 20 s, 40 cycles of denaturing at 95 °C for 1 s, and annealing/extending at 60 °C 20 s). Results were normalized to 18S and presented as a fold change relative to the treatment vehicle using the  $2^{-\Delta\Delta C_t}$  method, where the vehicle treated group was set to 1.

#### **Western blot**

Endothelial cells were lysed with 1X RIPA buffer (Cell Signaling Technology, Danvers, MA) supplemented with 1X protease/phosphatase inhibitor (Cell Signaling Technology). Total protein concentrations were determined by Bradford Assay with the Bio-Rad Protein Assay Dye reagent concentrate (Bio-Rad) following the manufacturer's instructions. Forty  $\mu$ g of protein was electrophoresed on a 4–12% polyacrylamide gel (Bio-Rad) and transferred to nitrocellulose membranes (Amersham Biosciences, Woburn, MA). Membranes were blocked for two hours at room temperature with 5% nonfat dry milk (Lab Scientific bioKEMIX Inc., Danvers, MA) and 3% bovine serum albumin (Thermo Fisher Scientific) in 1X Tris-Buffered Saline (Quality Biological, Gaithersburg, MD) containing 0.1% Tween-20 (TBS-T, Sigma). Blots were probed with antibodies with specificity to Zo-1, claudin-5, occludin, CYP3A4, PXR, or CAR overnight at 4 °C, washed with TBS-T, and probed with the appropriate secondary antibody for one hour at room temperature. Antibody details are provided in Table 1. All antibodies were titrated to determine optimal concentrations. Western Lightning Plus-ECL (PerkinElmer, Waltham, MA) was used as chemiluminescence substrate and the signal detected with the Azure Biosystems c600 Imager (Azure Biosystems, Dublin, CA). As a loading control, membranes were stripped with Restore Plus Western Blot Stripping

**Table 1** Details regarding antibody name, catalogue number, clone, concentration, and company from which it was obtained are provided for antibodies used in the study. Antibodies were knockout verified, are widely published on, and have been certifiably verified by the vendor

Antibody	Company	Catalogue Number	Clone	Concentration for Immunofluorescence	Concentration for Western Blot
GFAP(AF488)	Invitrogen	53-9892-82	GA5	10 µg/mL	
GLUT-1	Invitrogen	PA5-16,793	Poly	1:100	
CD71	Invitrogen	14-0719-82	OKT9	5 µg/mL	
PECAM(FITC)	Invitrogen	11-0311-82	390	5 µg/mL	
VE-cadherin	Invitrogen	14-1449-82	16B1	5 µg/mL	
Zo-1	Invitrogen	61-7300	Poly	10 µg/mL	1 µg/mL
Occludin	Invitrogen	71-1500	Poly	4 µg/mL	0.5 µg/mL
Claudin 5	Invitrogen	35-2500	4C3C2	1:25	1:1000
OAT1	Invitrogen	PA5-26,244	Poly	1:100	1:1000
OAT3	Invitrogen	PA5-76,143	Poly	1:100	1:1000
ENT1	Proteintech	11,337-1-AP	Poly	1:100	
ENT1	Invitrogen	PA5-116,461	Poly		1:500
OATP1A2	Invitrogen	PA5-42,445	Poly	1:100	1:1000
OATP2A1	Invitrogen	PA5-98,789	Poly	1:200	1:1000
BCRP	Novus	NBP2-22,124	3G8	1:200	1:2000
P-gp	Invitrogen	PA5-61,300	Poly	2 µg/mL	
P-gp	Abcam	ab261736	Poly		0.5 µg/mL
MRP1	Abcam	ab24102	MRPm5	1:50	1:200
MRP4	Cell Signaling	12,705	D2Q2O	1:200	1:1000
MRP5	Invitrogen	PA5-18,965	Poly	10 µg/mL	
MRP5	Abcam	Ab180724	Poly		1:1000
CYP3A4	Invitrogen	MA5-17,064	3H8	1:200	1:1000
PXR	Invitrogen	PA5-72,551	Poly	1:50	1:1000
CAR	R&D Systems	PP-N4111-00	N4111	10 µg/mL	2 µg/mL
AK1	Invitrogen	PA5-52,297	Poly	1 µg/mL	0.1 µg/mL
AK2	Proteintech	11,014-1-AP	Poly	1:200	1:1000
AK5	Invitrogen	PA5-53,933	Poly	1.2 µg/mL	0.09 µg/mL
AK6	Novus	NBP2-67,116	B1-F4	1:100	1:2000
B-Actin (HRP)	Cell Signaling	12,262	8H10D10		1:5000
Anti-rabbit (HRP)	Abcam	ab97051	Poly		1:2000
Anti-mouse (HRP)	Abcam	ab97023	Poly		1:2000
Anti-rabbit (AF488)	Invitrogen	A-11008	Poly	1 µg/mL	
Anti-mouse (AF488)	Invitrogen	A-11001	Poly	0.67 µg/mL	
Anti-goat (AF488)	Invitrogen	A-11078	Poly	1 µg/mL	

Buffer (Thermo Fisher Scientific) and reprobated with antibody against  $\beta$ -Actin HRP for one hour at room temperature. Densitometric analysis was performed using ImageJ (Version 1.53t, NIH, Bethesda, MD) to quantitate the band density (pixels, arbitrary units) for all evaluated proteins. Relative band intensity for each protein of interest was determined by calculating its pixel ratio with  $\beta$ -actin. The vehicle treated group was

set to 1 and the relative fold change in protein expression relative to vehicle determined.

#### Proteomics

Endothelial cells were treated with cocaine hydrochloride (10 µM) or vehicle for 24 h at 37 °C, 5% CO<sub>2</sub>, after which time whole cell proteins were extracted using a 5% sodium dodecyl sulfate and 50 mM triethylammonium bicarbonate lysis buffer. Protein concentration

was determined using the Pierce BCA Protein Assay Kit (Thermo Fisher Scientific) following the manufacturer's instructions. Proteins were digested into peptides using the S-Trap™ 96-well plate (ProtiFi, Fairport, NY) following the manufacturer's instructions. In brief, 100 µg of protein from each sample was solubilized in 5% SDS, reduced with 120 mM tris(2-carboxyethyl)phosphine (ProtiFi), alkylated using 500 mM methyl methanethio-sulfonate (ProtiFi), acidified with 1.2% phosphoric acid (ProtiFi), trapped on column, and then digested by 10 µg MS-grade trypsin (Thermo Scientific). Once peptides were eluted, they were dried under vacuum centrifugation (Eppendorf, Enfield CT) overnight, resuspended in 100 µl 0.1% formic acid in H<sub>2</sub>O (Thermo Fisher Scientific), and quantified using the Pierce Quantitative Colorimetric Peptide Assay kit (Thermo Scientific). Samples were diluted to 100 ng/µl and 2 µl were injected by an EasyNLC 1200 (Thermo Fisher Scientific) nanoflow liquid chromatography system coupled to a timsTOF Flex mass spectrometer (Bruker, Billerica, MA). Mobile phase A was 0.1% formic acid in H<sub>2</sub>O (Thermo Fisher Scientific) and mobile phase B was 0.1% formic acid (Thermo Fisher Scientific) in 80% acetonitrile/20% H<sub>2</sub>O (Thermo Fisher Scientific). Peptides passed through an Acclaim PepMap C18 100 Å, 3 µm, 75 µm×2 cm trap column (Thermo Scientific) followed by separation on a PepSep C18 100 Å, 1.5 µm, 75 µm×15 cm (Bruker) at a flow rate of 200 nl/min using the following 1 h gradient: 10%–35% B from 0 to 47 min, 35%–100% B from 47 to 55 min, 100% B from 55 min to 57 min, 100%–5% B from 57 min to 58 min, and 5% B from 58 min to 60 min. The trap column equilibration used a 9 µl at 3.0 µl/min flow rate and the separation column equilibration used a 12 µl at 3.0 µl/min flow rate. Additionally, 1 wash cycle of 20 µl and a flush volume of 100 µl were used. Peptides were ionized using the CaptiveSpray source, with a capillary voltage of 1500 V, dry gas flow of 3 l/min and temperature 180 °C. Data were acquired using a positive ion mode diaPASEF method with a mass range from 100–1700 m/z and 1/K<sub>0</sub> from 0.80 V<sub>s</sub>/cm<sup>2</sup> to 1.35 V<sub>s</sub>/cm<sup>2</sup> with 100 ms ramp time and 2 ms accumulation time. General tune parameters were: Funnel 1 RF=300 Vpp, idCID Energy=0 eV, Deflection Delta=70 V, Funnel 2 RF=200 Vpp, Multipole RF=500 Vpp, Ion Energy=5 eV, Low Mass=200 m/z, Collision Energy=10 eV, Collision RF=1500 Vpp, Transfer Time=60 µs, Pre Pulse Storage=12 µs, and Stepping turned off. Tims tune parameters were: D1=-20 V, D2=-160 V, D3=110 V, D4=110 V, D5=0 V, D6=55 V, Funnel1 RF=475 Vpp, and Collision Cell In=300 V. Resulting spectra were uploaded to Spectronaut 17.1 (Biognosys, Cambridge, MA). Peptides were identified and quantified using the directDIA analysis default settings with the proteotypicity filter set to “Only

Proteotypic” and a variable modification set to “methylation.” MS1 protein group quantifications and associated protein group UniProt numbers and molecular weights were exported from Spectronaut. MS1 protein group quantifications, UniProt numbers, and molecular weights were imported into Perseus for use of the proteomic ruler plug-in, as previously described [97]. The default proteomic ruler plug-in settings were used with histone proteomic ruler as the scaling mode, ploidy set to two, and total cellular protein concentration set to 200 g/l. Protein concentrations (nM) and copy numbers as estimated by the proteomic ruler were used for analysis.

### Flow cytometry

Endothelial cells were gently recovered from tissue culture plates using TrypLE Express (Invitrogen, Grand Island, NY) to maintain surface antigen expression for 10–15 min at 37 °C, 5% CO<sub>2</sub> as previously described [91]. After recovery, the cells were washed once with phosphate buffered saline (PBS, Gibco) and extracellular immunostaining performed. The cells were washed once with cold flow cytometry buffer (PBS supplemented with 2% Human Serum) (Corning, Manassas, VA) and 500,000 cells per tube were stained with fluorochrome-coupled antibodies specific for CD54/ICAM, CD31/PECAM-1, F11r/JAM-A, CD166/ALCAM, or corresponding isotype-matched negative control antibodies (BD Biosciences, Franklin Lakes, NJ) in the dark, on ice for 30 min. Antibody details are listed in Table 1. All antibodies were titrated to determine optimal concentrations for staining. Following staining, the cells were washed with cold flow cytometry buffer and fixed with 2% paraformaldehyde (Electron Microscopy Sciences, Hatfield, PA). The samples were stored at 4 °C wrapped in foil up to 1 week prior to flow cytometric analysis. Samples were filtered using BD FACS tubes with cell strainer caps with 35-µm pores (BD Biosciences) immediately before flow cytometric acquisition. At least 10,000 live, singlet events were acquired with a BD LSRFortessa cytometer and Diva software version 9 on the Windows 10 platform (BD Biosciences). Flow cytometric data were analyzed using FlowJo version 10.9 (FlowJo, Ashland, OR).

### Immunofluorescent microscopy

Endothelial cells were seeded ( $1.6 \times 10^4$  cells/dish) on 35 mm ibiTreat dishes (Ibidi USA, Madison, WI) coated with 0.2% gelatin, grown to 80% confluence, and treated with cocaine hydrochloride (10 µM). Following treatment, cells were fixed with 4% paraformaldehyde (Electron Microscopy Sciences) for 15 min. The cells were stained with wheat germ agglutinin conjugated to Texas red (Thermo Fisher Scientific) for 10 min to facilitate identification of cell morphology through staining of

the plasma membrane. Cells were then permeabilized in 0.01% Triton X-100 (Sigma) for one minute then blocked for two hours at room temperature in Dulbecco's phosphate-buffered saline without calcium or magnesium (DPBS) (Thermo Fisher Scientific) containing 5 mM ethylenediaminetetraacetic acid (EDTA) (Sigma), 1% fish gelatin (Sigma), 1% essentially immunoglobulin-free bovine serum albumin (Sigma), 1% heat-inactivated human serum AB (GeminiBio, Sacramento, CA), and 1% goat serum (Vector Laboratories, Newark, CA). Cells were probed with antibodies with specificity to Zo-1, OAT1, OAT3, ENT1, OATP1A2, OATP2A1, BCRP, P-gp, MRP1, MRP4, MRP5, CYP3A4, PXR, CAR, AK1, AK2, AK5 or AK6, overnight at 4 °C, washed three times with DPBS at room temperature, and probed with the appropriate Alexa Fluor 488 conjugated secondary antibody for one hour at room temperature. Isotype-matched controls, staining with only secondary antibodies, and unstained cells were used as negative controls and to account for autofluorescence and nonspecific signal. Antibody details are listed in Table 1. Cells were mounted with Ibbidi mounting medium containing DAPI as a counterstain to identify nuclei (Ibbidi USA, Madison, WI). Cells were imaged by fluorescent microscopy using the ECHO Revolution (San Diego, CA).

For evaluation of the BBB model, a surgical blade was used to outline the polycarbonate membrane from the tissue culture insert from the basolateral side, leaving only a small portion adhered to the insert. The polycarbonate membrane was carefully removed from the tissue culture insert, gently washed with PBS, and fixed with 4% paraformaldehyde (Electron Microscopy Sciences) for 20 min at 37 °C, 5% CO<sub>2</sub>. The polycarbonate membranes were placed into an eight-well chamber slide (Ibbidi USA), paying attention to place the apical or basolateral side facing downwards to stain the endothelial cells or astrocytes, respectively. The polycarbonate membranes were stained with wheat germ agglutinin conjugated to Texas red (Thermo Fisher Scientific) for 10 min to facilitate identification of cell morphology through staining of the plasma membrane. Cells on the polycarbonate membranes were then permeabilized in 0.01% Triton X-100 (Sigma) for one minute then blocked for two hours at room temperature in DPBS containing 5 mM EDTA (Sigma), 1% fish gelatin (Sigma), 1% essentially immunoglobulin-free bovine serum albumin (Sigma), 1% heat-inactivated human serum AB (GeminiBio, Sacramento, CA), and 1% goat serum (Vector Laboratories, Newark, CA). The polycarbonate membranes were probed with antibodies with specificity to GFAP or VE-Cadherin, overnight at 4 °C, washed three times with DPBS at room temperature, and probed with the appropriate Alexa Fluor 488 conjugated secondary antibody

for one hour at room temperature. Antibody details are listed in Table 1. All antibodies were titrated to determine optimal concentrations. Isotype-matched controls, staining with only secondary antibodies, and unstained membranes were used as negative controls and to account for autofluorescence of the polycarbonate membranes and nonspecific signal. The polycarbonate membranes were stained with Ibbidi mounting medium containing DAPI as a counterstain to identify nuclei (Ibbidi USA, Madison, WI). The polycarbonate membranes were imaged by fluorescent microscopy using the ECHO Revolution (San Diego, CA).

Images were acquired 1–15 days post fixation using the ECHO Revolution in the inverted mode with a 20X Plan Apo objective (with a 0.8 numerical aperture) where three channels were used: blue to identify nuclei, red to identify cell morphology, and green to identify the protein of interest. The appropriate focal plane along the Z-axis was determined manually prior to image acquisition. The signal to noise ratio was maximized by optimizing the appropriate exposure time and incident light intensity prior to image acquisition to prevent saturation and minimize background. Identical acquisition settings, including exposure time and intensity, were used for all treatment conditions where images were acquired on the same day to minimize batch effects due to fluorescent fading/quenching. Twenty images were acquired for all treatment conditions, with the exception of Zo-1 for which 10 images were taken and the BBB inserts where 3–5 images were taken. (FIJI is Just) ImageJ v1.54b (National Institutes of Health) was used for image quantification.

#### Efflux transporter activity assay

Efflux transporter activity was determined by cellular efflux of rhodamine 123 (10 μM, Thermo Fisher Scientific), Hoechst 33342 (5 μg/mL, Thermo Fisher Scientific), and monobromobimane (10 μM, Thermo Fisher Scientific), fluorescent substrates with specificity for P-gp, BCRP, and MRP4, respectively. It is important to note that we did not observe intracellular trapping of monobromobimane (Fig. 8B) or oxidative stress sufficient to induce cell death (data not shown) in our study. Further, while Hoechst 33342 is a well-established transport substrate of BCRP, evidence exists that there could also be mixed effects due to overlapping specificity with P-gp [98, 99].

Endothelial cells were incubated with fluorescent substrate for 1 h at 37 °C, 5% CO<sub>2</sub> to allow uptake into the cell, after which time fresh media added and the substrates allowed to efflux from the cells for four hours at 37 °C, 5% CO<sub>2</sub>. To evaluate the impact of cocaine on efflux transporter activity, endothelial cells were

pre-treated with 10  $\mu\text{M}$  cocaine hydrochloride for 24 h prior to addition of the fluorescent substrates. To evaluate the effect of PXR inhibition on efflux transporter activity, the endothelial cells were pre-treated with 10  $\mu\text{M}$  of the PXR-specific inhibitor resveratrol (Sigma) 24 h prior to addition of the fluorescent substrates. As a control, 10  $\mu\text{M}$  ritonavir (Sigma), fumitremorgin C (Sigma), and ceefourin 1 (Tocris Bioscience, Minneapolis, MN) were added concomitantly with the media change and served as known inhibitors of P-gp, BCRP, and MRP4, respectively. Vehicle treatment was used as a negative control. Following treatments, cells were washed with PBS, detached from tissue culture plates with 0.5% Trypsin–EDTA (Gibco), and the cells washed with PBS again. The cells were filtered using BD FACS tubes with cell strainer caps with 35- $\mu\text{m}$  pores (BD Biosciences) and immediately subject to flow cytometric acquisition where at least 10,000 singlet events were acquired with a BD LSRFortessa cytometer and Diva software version 9 on the Windows 10 platform (BD Biosciences). Flow cytometric data were analyzed using FlowJo version 10.9 (FlowJo, Ashland, OR).

#### CYP3A4 metabolic activity assay

Endothelial cells were plated in 96-black microplate with clear flat bottom (Corning, NY) coated with 0.2% gelatin (Thermo Fisher Scientific) at a density of 5,000 cells per well and cultured overnight at 37 °C, 5% CO<sub>2</sub> in M199C. After overnight culture, endothelial cells were pre-treated with cocaine hydrochloride (10  $\mu\text{M}$ ), positive control rifampicin (1  $\mu\text{M}$ , Sigma) the PXR-specific inhibitor resveratrol (10  $\mu\text{M}$ , Sigma), or vehicle control. Twenty-four hours post treatment, the cells were washed twice with PBS and incubated with 2  $\mu\text{M}$  of the CYP3A4 fluorogenic probe substrate, 7-benzyloxy-4-trifluoromethylcoumarin (BFC, Sigma), for 90 min at 37 °C, 5% to permit its oxidative enzymatic conversion to the fluorescent metabolite 7-hydroxy-4-trifluoromethylcoumarin (HFC). After this period, fluorometric quantitation was performed using the Spectra Max iD5 (Molecular Devices) microplate reader at excitation and emission wavelengths of 405/535 nm.

Baseline subtraction was performed by subtracting the RFU at the initial timepoint (0) for vehicle treatment from all other conditions. The ratio between RFU and time (minutes) was taken to calculate CYP3A4 velocity (RFU/minutes). Only the linear portion of the curve (0–20 min) was used for quantitative analysis.

#### Statistical analysis

Three independent experiments comprised of four technical replicates were performed for ART BBB extravasation assays. Seven independent experiments comprised

of three technical replicates were performed for BBB permeability assays. Samples for qRT-PCR's were run in triplicate. Liquid chromatography/mass spectrometry and proteomic assays were run with three independent sample injections. All remaining in vitro experiments were repeated in at least  $n \geq 5$  independent experiments.

Raw files without compression were used for immunofluorescent microscopy quantification where 250–500 cells were analyzed for each treatment, with the exception of Zo-1 where 70–100 cells were used. Three regions of interest (ROI) were used to facilitate quantitation of fluorescent signal: background, nuclei, and cells. The background signal was determined using the red channel where rectangular ROI's were drawn in regions containing no cells. Background ROI's were superimposed onto the green channel for the protein of interest and the average intensity was measured. Nuclei were segmented from the background using the blue channel and creating a binary image using Otsu thresholding. Nuclear ROI's were created using the binary image and the particle analyzer in FIJI (size > 1000-pixel units, circularity between 0.00–1.00). Nuclear ROI's were superimposed onto the green channel for the protein of interest and average intensity was measured. The red image was used to facilitate identification of cell boundaries and ROI's were drawn freehand around clusters of cells. The cellular ROI's were superimposed onto the green channel illuminating the protein of interest and average intensity was measured. The average intensity of the local background for each image was subtracted from the average intensity measurement of each ROI to determine the relative fluorescent units for each protein of interest.

Details regarding the number of experimental performed are included in all figure legends. All data are graphically represented as mean  $\pm$  SD. Statistical analyses were performed using Prism software 10.0 GraphPad Software, Inc., San Diego, CA). A D'Agostino-Pearson normality test was performed to evaluate whether the data fit a Gaussian distribution. When the data were normally distributed, a two-tailed parametric T-test ( $n=2$  groups) or a one-way ANOVA test (for  $\geq 3$  groups) was performed. When the data were not normally distributed, a Mann–Whitney test ( $n=2$  groups) was performed. Of note, all data where  $\geq 3$  groups were compared were normally distributed. When present, the vehicle treatment condition served as the reference group for multiple comparisons analyses in the one-way ANOVA test. \* $p \leq 0.05$ . \*\* $p \leq 0.01$ . \*\*\* $p \leq 0.001$ .

#### Results

##### FTC, TFV, and DTG Differentially cross the BBB

ART access to the CNS is an important public health concern as it contributes to maintenance of the brain as

a viral reservoir and increases risk for neurologic sequelae, including cognitive and mood disorders in people living with HIV. While it is clear that ART enters the CNS compartment, albeit to a lower extent as compared to plasma and peripheral organs [7, 100–111], the precise mechanisms at the BBB that facilitate this remain poorly understood. To address this, we used primary human brain microvascular endothelial cells and primary human astrocytes to develop an *in vitro* model of the human BBB. In this system, endothelial cells and astrocytes express proteins present *in vivo*, notably the transferrin receptor, claudin-5, glucose transporter 1, VE-cadherin, occludin, PECAM-1, Zo-1, and GFAP (Additional file 1: Figure S1). Importantly, we demonstrated previously that this BBB model is dynamically regulated in response to inflammatory and angiogenic stimuli in an expected fashion [91].

The BBB model is generated by seeding endothelial cells into the upper, apical compartment while astrocytes grow on the basolateral underside for a period of three days until confluence is reached. During this time, the astrocytes extend their endfeet processes to make physical contact with the endothelia, effectively sealing the barrier [87, 88] (Additional file 1: Figure S2A, C-F). This model has high transendothelial electrical resistance and is impermeable to endogenous molecules excluded from an intact BBB *in vivo*, including inulin [87, 88] and albumin (Additional file 1: Figure S2B).

We used this BBB model previously to evaluate immune cell migration in the context of HIV [86, 89, 90, 112]. Now, we leverage this system to evaluate the ability of three first-line ART drugs to cross the BBB: FTC, TFV, and DTG. Each ART drug (10  $\mu$ M) was added to the apical portion of the model and allowed to pass to the basolateral chamber for 24 h, after which time the media was collected and the concentration that passed determined by liquid chromatography/mass spectrometry. FTC and TFV readily crossed the BBB (Fig. 1). However, FTC concentrations were considerably lower than TFV, at  $792.2 \pm 136.3$  versus  $1183 \pm 142.9$  ng/mL, respectively ( $p=0.0134$ , one-way ANOVA). Of note, these concentrations exceed plasma maximum concentrations observed clinically [113–120]. In contrast, DTG was below the detectable limit of 100 ng/mL and therefore the concentration of drug that passed into the basolateral chamber was too low to quantitate (Fig. 1). These findings demonstrate that, while ART can cross the BBB, differing drugs have distinct propensities to enter the CNS.

#### Cocaine selectively modulates FTC and TFV extravasation across the BBB

To evaluate the impact of comorbid substance use on ART availability in the CNS, BBB extravasation

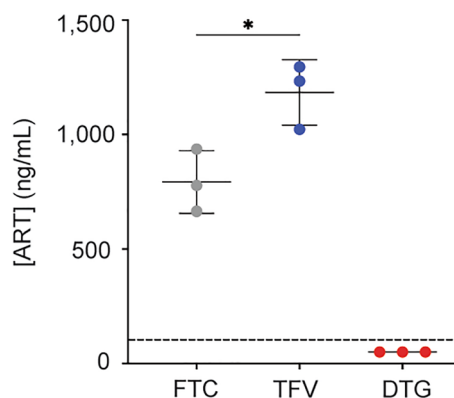


**Fig. 1** Differential ART Propensity to Cross the BBB. FTC (grey), TFV (blue), and DTG (red) (all at 10  $\mu$ M) were added to the apical portion of the BBB model and allowed to extravasate into the basolateral portion for 24 h at 37  $^{\circ}$ C, 5%  $\text{CO}_2$ . After this period of time, the media in the basolateral compartment was collected and the concentration of each ART drug that passed was measured by liquid chromatography/mass spectrometry. Dashed line denotes quantitative limit of detection for DTG. Three independent experiments (represented by individual dots), that included seven technical replicates, were performed. Data are represented as mean  $\pm$  standard deviation. \* $p < 0.05$ . One-way ANOVA was performed

experiments were performed in the presence and absence of cocaine. The ability of ART to cross the BBB in the presence of LPS, a potent immune stimulus and inflammatory agent, was also performed as it is an important modulator of barrier function [121–129]. FTC, TFV, and DTG (10  $\mu$ M) were added to the apical portion of the BBB model in the presence and absence of cocaine (10  $\mu$ M) or LPS (10 ng/mL) and allowed to pass to the basolateral chamber for 24 h, after which time the media was collected and the ART concentration that passed determined by liquid chromatography/mass spectrometry. Cocaine increased the mean FTC concentration in the basolateral compartment by  $268.4 \pm 6.5$  ng/mL ( $p=0.0006$ , T-test, Fig. 2A). While cocaine also impacted the concentration of TFV that passed the BBB, it had an opposing effect and decreased its presence by  $293.2 \pm 26.7$  ng/mL ( $p=0.0027$ , T-test, Fig. 2B). Interestingly, LPS had an inconsistent effect (Fig. 2C-D), where it caused a mean increase of  $317.6 \pm 566.4$  ng/mL for FTC ( $p=0.4339$ , T-test) and a decrease of  $190.2 \pm 202.2$  ng/mL for TFV ( $p=0.2449$ , T-test) that crossed the BBB. This suggests a specificity for cocaine's impact on ART extravasation across the BBB, rather than a general mechanism that broadly occurs. The concentrations of DTG that passed the BBB in the presence of cocaine and LPS were below quantifiable limits (data not shown).

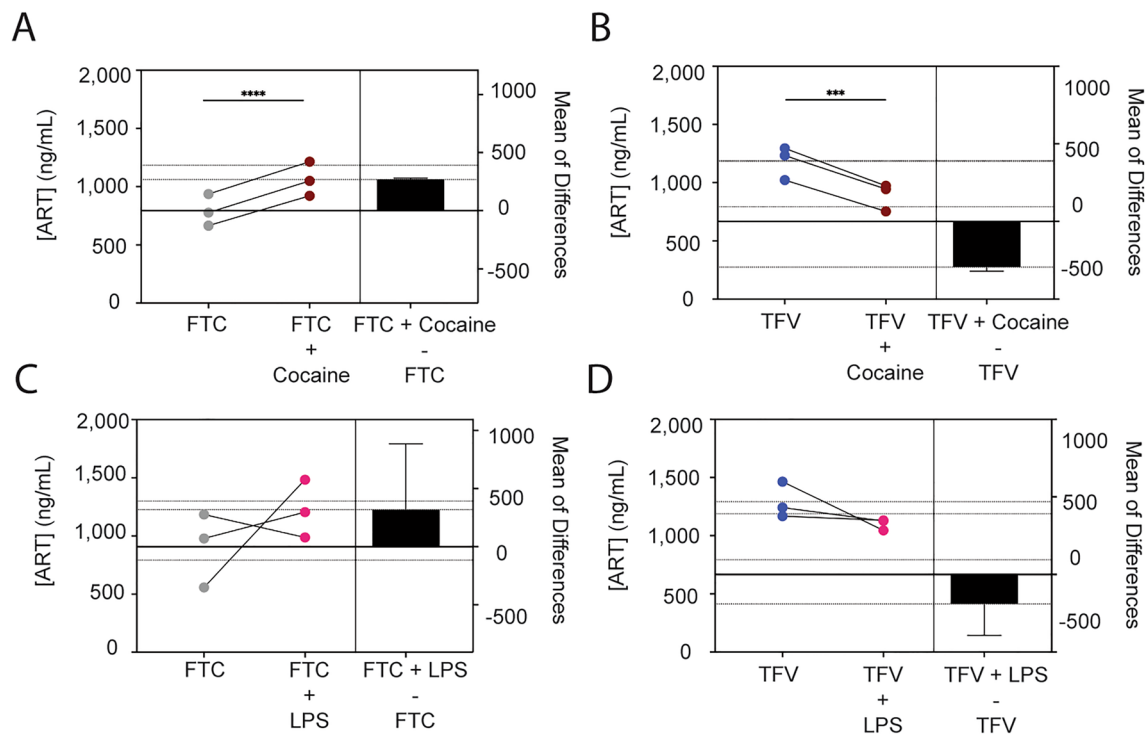


**Fig. 2** Cocaine, But Not LPS, Modulates ART Extravasation Across the BBB. FTC (grey, **A** and **C**) and TFV (blue, **B** and **D**) (both at 10  $\mu$ M) were added to the apical portion of the BBB model and allowed to extravasate into the basolateral portion in the presence or absence of cocaine (10  $\mu$ M, burgundy, **A–B**) or LPS (10 ng/mL, fuchsia, **C–D**) for 24 h at 37  $^{\circ}$ C, 5% CO<sub>2</sub>. The media in the basolateral compartment was collected and the concentration of each ART drug that passed was measured by liquid chromatography/mass spectrometry. Three independent experiments (represented by individual dots), that included seven technical replicates, were performed. Estimation plots are shown where the left y-axis denotes ART concentration (ng/mL) and the right y-axis reflects the effect size (black bar), which is the difference between means of each condition. Data are represented as mean  $\pm$  standard deviation. \*\*\* $p$  < 0.001. \*\*\*\* $p$  < 0.0001. Paired T-test was performed

### Cocaine does not impact BBB permeability, cytokine production, or key structural endothelial proteins

The differential selectivity by which FTC, TFV, and DTG crossed the BBB and the specificity for cocaine's modulation of these processes, suggests well-regulated mechanisms are elicited that impact ART CNS concentrations. Nonetheless, it is important to consider that diminished BBB integrity may also occur, which would have an additional impact on ART extravasation. To test this possibility, we first evaluated BBB permeability to albumin, the most abundant plasma protein, which is unable to cross an intact BBB under homeostatic conditions. However, it can readily bypass breaches in a compromised BBB where it enters the CNS and contributes to pathology. As such, albumin is used clinically as an index of BBB damage.

We evaluated permeability of the BBB model to EBA, where albumin-conjugated Evans blue dye that passed to the basolateral chamber was quantitated spectrophotometrically (Additional file 1: Figure S2B). The BBB was treated with cocaine (10  $\mu$ M), LPS (10 ng/mL), or vehicle control for 24 h, after which time permeability to EBA was evaluated. To our surprise, BBB models treated

with cocaine had only a slight increase in permeability (Fig. 3A), as evidenced by a 50% increase ( $p=0.1244$ , one-way ANOVA) in the optical density at 620 nm ( $OD_{620}$ ), as compared to vehicle treatment. There was an even smaller impact of LPS on BBB permeability as treatment caused only a 13% increase in the  $OD_{620}$  ( $p=0.8387$ , one-way ANOVA), as compared to vehicle. In contrast, a complete breach of the BBB would have permitted all the EBA dye into the basolateral chamber and resulted in a 580% increase in the  $OD_{620}$  ( $p<0.0001$ , one-way ANOVA, Fig. 3A), as compared to vehicle treatment.

As albumin is a large tracer of 67 kDa that can only cross a substantially impaired BBB, we evaluated whether cocaine impacted the barrier integrity more subtly by diminishing key interendothelial junctions that promote transcellular integrity. First, we treated endothelial cells with cocaine (10  $\mu$ M), or vehicle, between 0.5 to 24 h and evaluated Zo-1 by qRT-PCR (Fig. 3B). While there was, on average, a 20.4% decrease ( $p=0.2706$ – $0.8724$ , one-way ANOVA) in Zo-1 mRNA between 0.5 to 6 h, levels were restored to near basal levels by 24 h (3% decrease in Zo-1 mRNA,  $p=0.9997$ , one-way ANOVA). A similar

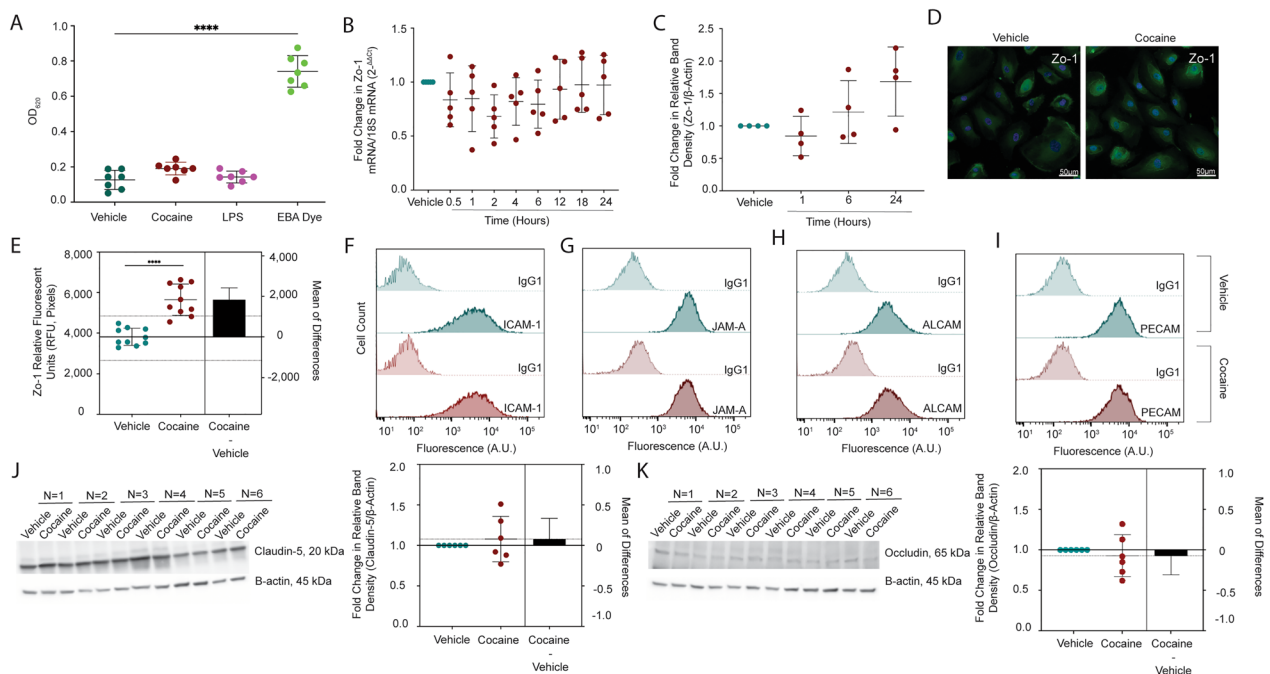


**Fig. 3** Cocaine Does Not Disrupt BBB Integrity. **A** BBB models were treated with cocaine (10  $\mu$ M, burgundy), LPS (10 ng/mL, fuchsia), or vehicle (teal) for 24 h, after which time permeability to EBA dye was performed. EBA was added to the apical portion of the BBB for 30 min at 37  $^{\circ}$ C, 5%  $\text{CO}_2$ , the media in the bottom collected, and evaluated spectrophotometrically at  $\text{OD}_{620}$ . EBA dye alone (green) was used as a positive control to represent maximal BBB permeability. Seven individual experiments were performed (represented by individual dots). Data are represented as mean  $\pm$  standard deviation. \*\*\*\* $p < 0.0001$ . One-way ANOVA was performed. **B** qRT-PCR was performed to evaluate Zo-1 mRNA following 0.5–24 h treatment with cocaine (10  $\mu$ M, burgundy). The  $2^{-\Delta\Delta\text{Ct}}$  method was performed to evaluate fold change in Zo-1 mRNA relative to 18S mRNA where vehicle treatment (teal) was set to 1. Five individual experiments were performed (represented by individual dots). Data are represented as mean  $\pm$  standard deviation. **C** Western blot was performed to evaluate Zo-1 total protein expression following 1, 6, and 24 h treatment with cocaine (10  $\mu$ M, burgundy). Blots were stripped and reprobed to evaluate  $\beta$ -actin for protein normalization. The fold change in relative band intensity for Zo-1/ $\beta$ -actin was determined by densitometry where vehicle treatment (teal) was set to 1. Four individual experiments were performed (represented by individual dots). Data are represented as mean  $\pm$  standard deviation. **D** Immunofluorescent microscopy was performed to evaluate Zo-1 (green) following treatment with cocaine (10  $\mu$ M, right) or vehicle (left) for 24 h. DAPI was used to visualize nucleus (blue). One paired representative image, out of 10 individual images, are shown. All scale bars = 50  $\mu$ m. **E** Quantification of the fluorescent signal from Zo-1 immunofluorescent microscopy was performed for endothelial cells treated with cocaine (10  $\mu$ M, burgundy) or vehicle (teal) for 24 h. Ten independent experiments (represented by individual dots) were performed. Estimation plots are shown where the left y-axis denotes relative fluorescent intensity (RFU, pixels) and the right y-axis reflects the effect size (black bar), which is the difference between means of each condition. Data are represented as mean  $\pm$  standard deviation. \*\*\*\* $p < 0.0001$ . Unpaired T-test was performed. **F–I** Flow cytometry was performed to evaluate cell surface expression of **(F)** ICAM-1, **(G)** JAM-A, **(H)** ALCAM, and **(I)** PECAM following 24-h treatment with cocaine (10  $\mu$ M, burgundy) or vehicle (teal). Fluorescence (arbitrary units) was evaluated for the specific protein of interest or following staining with an irrelevant, nonspecific isotype matched negative control antibody (IgG1). Data from one representative experiment, out of four individual experiments, are shown. **J–K** Western blot was performed to evaluate **(J)** claudin-5 and **(K)** occludin total protein expression in endothelial cells following 24-h treatment with cocaine (10  $\mu$ M, burgundy) or vehicle (teal).  $\beta$ -actin was used for protein normalization. Western blots demonstrating six independent experiments are shown (left). The fold change in relative band intensity for each protein relative to  $\beta$ -actin was determined by densitometry where vehicle treatment (teal) was set to 1 (right). Six independent experiments (represented by individual dots) were performed. Estimation plots are shown where the left y-axis denotes fold change in relative band intensity for the protein of interest relative to  $\beta$ -actin and the right y-axis reflects the effect size (black bar), which is the difference between means of each condition. Data are represented as mean  $\pm$  standard deviation

pattern occurred at the protein level evaluated by Western blot analysis (Fig. 3C), where the relative band density for Zo-1 decreased at 1 h (16% decrease,  $p = 0.8944$ , one-way ANOVA), was later restored, and even trended towards an increase as compared to vehicle treatment by 24 h (68% increase,  $p = 0.0717$ , one-way ANOVA). As this was unexpected, we evaluated Zo-1 more comprehensively by immunofluorescent microscopy analysis

following 24 h of cocaine (10  $\mu$ M) or vehicle treatment. Confirming the Western blot, cocaine induced a 48% increase ( $p < 0.0001$ , T-test) in Zo-1 relative fluorescent unit (RFU) intensity after 24 h of cocaine treatment, compared to vehicle (Fig. 3D–3E).

We next examined the impact of cocaine on cytokines involved in eliciting innate immune responses. The apical portion of the BBB model was treated with cocaine

(10  $\mu$ M), LPS (100 ng/mL) as a positive control, or vehicle for 24 h. Following treatment, the supernatant was collected from the apical portion and thirteen cytokines involved in the innate immune response were evaluated. Cocaine did not promote cytokine production at the BBB, including IL-1 $\beta$  (Fig. 4A), IL-6 (Fig. 4B), TNF- $\alpha$  (Fig. 4C), IP-10 (Fig. 4D), IFN- $\lambda$ 1 (Fig. 4E), IL-8 (Fig. 4F), IL-12p70 (Fig. 4G), IFN- $\alpha$ 2 (Fig. 4H), IFN- $\beta$  (Fig. 4I), GM-CSF (Fig. 4J), IL-10 (Fig. 4K), IFN- $\lambda$ 2/3 (data not shown), and IFN- $\gamma$  (data not shown). In contrast, LPS produced a robust immune response for all evaluated cytokines (Fig. 4 and data not shown). Importantly, neither cocaine nor LPS promoted endothelial cell death following 0.5 or 24 h of exposure (Additional file 1: Figure S3).

As cytokine production is an important neuroinflammatory mechanism that may impact BBB integrity, we sought to evaluate permeability using 4 kDa FITC-dextran. Of note, this tracer is substantially smaller than that of EBA enabling for the sensitive determination of even minor perturbations to BBB integrity. Similar to that which occurred with our EBA analyses (Fig. 3A), neither cocaine nor LPS altered BBB integrity. BBB models treated with cocaine had only a minor effect on permeability (Fig. 4L), as evidenced by a 5% decrease ( $p=0.1507$ , one-way ANOVA) in fluorescence, as compared to vehicle treatment. There was a comparable impact of LPS on BBB permeability as treatment caused only an 8% decrease in fluorescence ( $p=0.1419$ , one-way ANOVA), as compared to vehicle. Of note, this experiment used a tenfold higher concentration of LPS at 100 ng/mL, rather than 10 ng/mL used in the EBA determination. Nevertheless, the BBB models maintained impermeability. In contrast, a complete breach of the BBB would have permitted all the 4 kDa FITC-dextran into the basolateral

chamber and resulted in a 40% increase in fluorescence ( $p<0.0001$ , one-way ANOVA, Fig. 3A), as compared to vehicle treatment.

We also evaluated the impact of cocaine on additional tight junction and adhesion molecule proteins that serve to maintain BBB integrity by flow cytometry. Endothelial cells were treated with cocaine (10  $\mu$ M) or vehicle for 24 h, the cells gently removed from adherent culture with TrypLE to maintain surface antigens [91], and immunostained and analyzed by flow cytometry. Histogram plots, representative of four independent experiments, demonstrated that cocaine did not alter the cell surface expression of intercellular adhesion molecule 1 (ICAM-1), junctional adhesion molecule A (JAM-A), activated leukocyte cell adhesion molecule (ALCAM), and platelet-endothelial cell adhesion molecule (PECAM-1) (Fig. 3F-I), as compared to vehicle treatment. In addition to the cell surface markers, we evaluated two tight junction molecules essential for BBB integrity, claudin-5 and occludin, by Western blot and determined that cocaine had an inconsistent and marginal impact on their expression with a 7% increase ( $p=0.5104$ , T-test) and 7% decrease ( $p=0.5128$ , T-test) in relative band density, respectively (Fig. 3J-K).

Finally, we aimed to evaluate the global impact of cocaine on proteins involved in maintaining endothelial cell junctions. To accomplish this, we performed untargeted proteomics following 24 h of treatment with cocaine (10  $\mu$ M) or vehicle. Of the 4,831 identified proteins, cocaine modulated only 12 proteins relating to BBB integrity (Table 2). Of these, the most substantially impacted was carcinoembryonic antigen-related cell adhesion molecule 1 (CEACAM1), which cocaine induced a 78% increase in copy number ( $p=0.0035$ ,

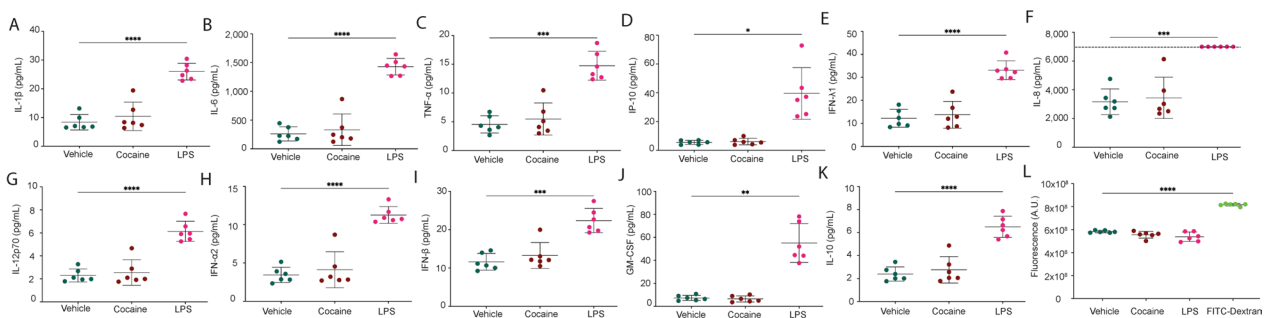


**Fig. 4** LPS, But Not Cocaine, Induces Cytokine Production at the BBB Which Does Not Disrupt BBB Integrity. BBB models were treated with cocaine (10  $\mu$ M, burgundy), LPS (100 ng/mL, fuchsia), or vehicle (teal) for 24 h, after which time (A-K) supernatants were collected for cytokine determination or (L) permeability to 4 kDa FITC-Dextran was performed. (A-K) Multiplexed cytokine analysis was performed by flow cytometry to evaluate (A) IL-1 $\beta$ , (B) IL-6, (C) TNF- $\alpha$ , (D) IP-10, (E) IFN- $\lambda$ 1, (F) IL-8, (G) IL-12p70, (H) IFN- $\alpha$ 2, (I) IFN- $\beta$ , (J) GM-CSF, and (K) IL-10. Dashed line denotes quantitative limit of detection for IL-8. (L) Four kDa FITC-Dextran was added to the apical portion of the BBB for 30 min at 37  $^{\circ}$ C, 5% CO $_2$ , the media in the bottom collected, and evaluated by a fluorescence microplate reader. FITC-Dextran alone (green) was used as a positive control to represent maximal BBB permeability. Six individual experiments were performed (represented by individual dots). Data are represented as mean  $\pm$  standard deviation. \*\* $p < 0.01$ . \*\*\* $p < 0.001$ . \*\*\*\* $p < 0.0001$ . One-way ANOVA was performed

**Table 2** Protein copy number and concentration following 24-h treatment with cocaine (10  $\mu$ M) or vehicle as determined by proteomics analysis

Protein	Vehicle		Cocaine	
	Copy Number	Concentration (nM)	Copy Number	Concentration (nM)
CEACAM1	59,626 $\pm$ 10,789	43.9 $\pm$ 7.5	106,220 $\pm$ 7,458**	86.6 $\pm$ 4.4**
COL6A1	206,854 $\pm$ 12,118	152.2 $\pm$ 3.7	131,021 $\pm$ 14,120**	106.9 $\pm$ 11.7**
CTSB	8,484,178 $\pm$ 416,822	6,252.0 $\pm$ 355.4	6,593,383 $\pm$ 408,852**	5,377.0 $\pm$ 230.0*
HPX	6,543,012 $\pm$ 138,928	4,821.0 $\pm$ 139.0	4,814,035 $\pm$ 116,364****	3,931.0 $\pm$ 184.8**
ICAM	676,996 $\pm$ 14,380	499.0 $\pm$ 24.0	721,746 $\pm$ 23,606*	588.8 $\pm$ 7.0**
MIF	3,493,966 $\pm$ 119,612	2,573.0 $\pm$ 39.4	4,902,856 $\pm$ 535,590*	3,996.0 $\pm$ 358.4**
PECAM	1,202,038 $\pm$ 59,972	885.6 $\pm$ 46.24	956,743 $\pm$ 10,063**	780.8 $\pm$ 9.6*
PICALM	1,014,023 $\pm$ 21,188	747.1 $\pm$ 20.5	788,182 $\pm$ 30,189**	643.2 $\pm$ 25.7**
NRP2	287,851 $\pm$ 21,441	212.0 $\pm$ 13.9	186,651 $\pm$ 2,301**	152.3 $\pm$ 3.6**
VTN	1,208,330 $\pm$ 68,554	890.8 $\pm$ 65.2	862,826 $\pm$ 6,116****	704.3 $\pm$ 20.8**
VWF	584,018 $\pm$ 20,536	430.1 $\pm$ 9.7	484,891 $\pm$ 17,129**	395.6 $\pm$ 11.0*

Mean  $\pm$  standard deviation are shown. Asterisks indicate statistical significance in cocaine treated cells relative to vehicle. Paired T-test. COL6A1, Collagen Type VI Alpha 1 Chain. CTSB Cathepsin B. HPX Hemopexin. MIF Macrophage Migration Inhibitory Factor. PICALM Phosphatidylinositol Binding Clathrin Assembly Protein. NRP2 Neuropilin 2. VTN Vitronectin. VWF Von Willebrand Factor. \* $p < 0.05$ . \*\* $p < 0.01$ . \*\*\* $p < 0.001$ . \*\*\*\* $p < 0.0001$

T-test) and a 97% increase in intracellular concentration ( $p = 0.0010$ , T-test), as compared to vehicle. The impact on CEACAM1 was atypical, however, as cocaine had a smaller impact on the remaining 11 proteins that ranged from a 6–40% change in copy number and an 8–55% change in intracellular concentration (Table 2). Together, these data suggest that in our system, cocaine does not substantially impact proteins involved in maintaining BBB integrity, does not increase permeability, and that its impact on ART extravasation into the CNS occurs through other mechanisms.

#### Cocaine decreases PXR, the master regulator of drug transporters and metabolizing enzymes

As cocaine did not impact BBB integrity, we sought to evaluate the mechanisms by which it affected ART CNS access. We hypothesized that cocaine regulated cellular processes contributing to drug transport and metabolism at the BBB. To address this hypothesis, we turned our attention to PXR and CAR: transcription factors that serve key roles in regulating drug transport and metabolism following induction by xenobiotics in efforts to detox the cell (Fig. 5A). We first performed Western blot to evaluate total protein levels in cell lysates obtained following 24-h treatment with cocaine (10  $\mu$ M) or vehicle and found that cocaine caused a 23% decrease in the relative band intensity for PXR ( $p < 0.0001$ , T-test), as compared to vehicle (Fig. 5B, 5D). Interestingly, this effect was specific to PXR as cocaine induced only a 7% decrease in the relative band intensity for CAR ( $p = 0.3133$ , T-test,

Fig. 5C, 5E). We confirmed these findings by immunofluorescence and found a similar cocaine-induced decrease in PXR (24% decrease in fluorescent signal,  $p < 0.0001$ , T-test, Fig. 5F, 5H), which did not occur for CAR (1% decrease in fluorescent signal,  $p = 0.9081$ , T-test, Fig. 5G-I).

We next evaluated the nuclear presence of PXR and CAR by immunofluorescent microscopy, as their transcriptional regulatory functions require translocation to the nucleus to affect drug transport and metabolism genes. The fluorescent signal for each respective protein that colocalized with DAPI was separated from that which occurred in the cytoplasm to facilitate analysis of PXR and CAR specifically in the nucleus. Interestingly, the PXR fluorescent signal in vehicle treated cells was higher in the nucleus (Fig. 6A-D), as compared to that which occurred in the entire cell (Fig. 5F-I), having a mean RFU of 12,349  $\pm$  1,222 versus 4,840  $\pm$  822, respectively. A similar effect occurred for CAR where the nuclear RFU was 6,896  $\pm$  1,302 while it was only 1,539  $\pm$  249.7 in the cytoplasm. Similar to that which occurred in the entire cell (Fig. 5H), cocaine decreased the nuclear PXR RFU by 29% ( $p < 0.0001$ , T-test) while having a 1% ( $p = 0.7959$ , T-test) increase in nuclear CAR RFU (Fig. 6B, D).

To characterize the effect of cocaine on PXR more comprehensively, we performed a dose response evaluating cocaine concentrations between 0.01–100  $\mu$ M. Interestingly, the cocaine-mediated decrease of PXR occurred in a dose-independent fashion (Fig. 6E). All subsequent experiments were performed at a cocaine concentration of 10  $\mu$ M in agreement with plasma levels that occur in

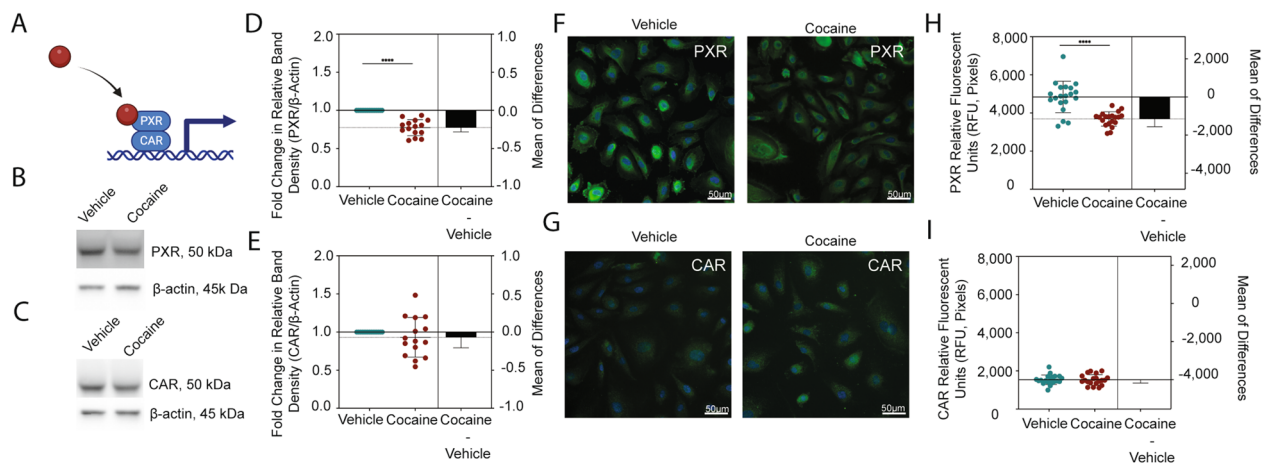


**Fig. 5** Cocaine Decreases PXR, But Not CAR, in Endothelial Cells. **A** Schematic representation depicting the transcriptional activity of PXR and CAR following ligand binding. **(B–C)** Western blot was performed to evaluate **(B)** PXR and **(C)** CAR following 24-h treatment with cocaine (10  $\mu$ M) or vehicle.  $\beta$ -actin was used for protein normalization. One western blot, representative of 15 independent experiments, is shown. **(D–E)** The fold change in relative band intensity for **(D)** PXR/ $\beta$ -actin and **(E)** CAR/ $\beta$ -actin was determined by densitometry where vehicle treatment (teal) was set to 1 (right). Fifteen independent experiments (represented by individual dots) were performed. Estimation plots are shown where the left y-axis denotes fold change in relative band intensity for the protein of interest relative to  $\beta$ -actin and the right y-axis reflects the effect size (black bar), which is the difference between means of each condition. Data are represented as mean  $\pm$  standard deviation. \*\*\*\* $p < 0.0001$ . Unpaired T-test was performed. **(F–G)** Immunofluorescent microscopy was performed to evaluate **(F)** PXR or **(G)** CAR (green) following treatment with cocaine (10  $\mu$ M, right) or vehicle (left) for 24 h. DAPI was used to visualize nucleus (blue). One paired representative image, out of 20 individual images, are shown. All scale bars = 50  $\mu$ m. **(H–I)** Quantification of the fluorescent signal from **(H)** PXR and **(I)** CAR immunofluorescent microscopy was performed for endothelial cells treated with cocaine (10  $\mu$ M, burgundy) or vehicle (teal) for 24 h. Twenty independent experiments (represented by individual dots) were performed. Estimation plots are shown where the left y-axis denotes relative fluorescent intensity (RFU, pixels) and the right y-axis reflects the effect size (black bar), which is the difference between means of each condition. Data are represented as mean  $\pm$  standard deviation. \*\*\*\* $p < 0.0001$ . Unpaired T-test was performed

a clinical setting [96]. We next evaluated whether there was a temporal effect of cocaine by treating cells with 10  $\mu$ M cocaine from 0.5–24 h. We determined there was a biphasic response, wherein cocaine significantly decreased PXR between 0.5–8 h, which was restored at 12 and 18 h, and decreased again at 24 h. (Fig. 6E–F). All subsequent experiments were performed with 24-h treatment to be consistent with ART clinical dosing regimens.

We next wanted to evaluate the specificity of the cocaine-mediated decrease in PXR. To accomplish this, we treated endothelial cells with cocaine, its minor metabolite norcocaine (10  $\mu$ M), its major metabolite benzoylecgonine (10  $\mu$ M), or vehicle for 24 h and evaluated PXR by Western blot. As before, cocaine caused a 24% decrease ( $p = 0.0005$ , one-way ANOVA) in the relative band intensity of PXR (Fig. 6G). However, this did not occur for its metabolites. Indeed, norcocaine caused only an 8% increase ( $p = 0.8612$ , one-way ANOVA) while benzoylecgonine had a 20% decrease ( $p = 0.2093$ , one-way ANOVA) in the relative band intensity of PXR. While benzoylecgonine's effects on PXR were most similar to cocaine, they occurred inconsistently and had a large standard deviation of 34%. There was a dose-independent lack of response of norcocaine and benzoylecgonine on PXR between 0.01–100  $\mu$ M (data not shown).

### Cocaine regulates drug transporter expression and activity

Cocaine's modulation of PXR, but not CAR, has implications for drug transport across the BBB. To characterize this further, we evaluated the impact of cocaine on ten drug transporters known to interact with ART, or whose substrate structural similarity indicates the potential to impact ART tissue availability. We focused on five influx transporters, as well as five transporters involved in efflux, and determined that cocaine modulated eight of the ten proteins (Fig. 7). Overall, cocaine decreased drug transporter expression, as compared to vehicle, where it promoted a loss of RFU for BCRP (18%,  $p = 0.0166$ , T-test), ENT1 (49%,  $p < 0.0001$ , T-test), MRP4 (23%,  $p = 0.0006$ , T-test), OAT1 (45%,  $p < 0.0001$ , T-test), OAT3 (17%,  $p < 0.0001$ , T-test), OATP1A2 (24%,  $p < 0.0001$ , T-test), and P-gp (24%,  $p < 0.0001$ , T-test). OATP2A1 was the only evaluated transporter that had an increased RFU (66%,  $p < 0.0001$ , T-test) following cocaine treatment.

Intrigued by the implications of cocaine modulating ART transport across the BBB, we next sought to evaluate whether there were functional consequences for the altered presence of the influx and efflux proteins. We focused on three efflux transporters known to interact with ART that are modulated by PXR: BCRP, MRP4, and P-gp. To accomplish this, we pre-treated endothelial

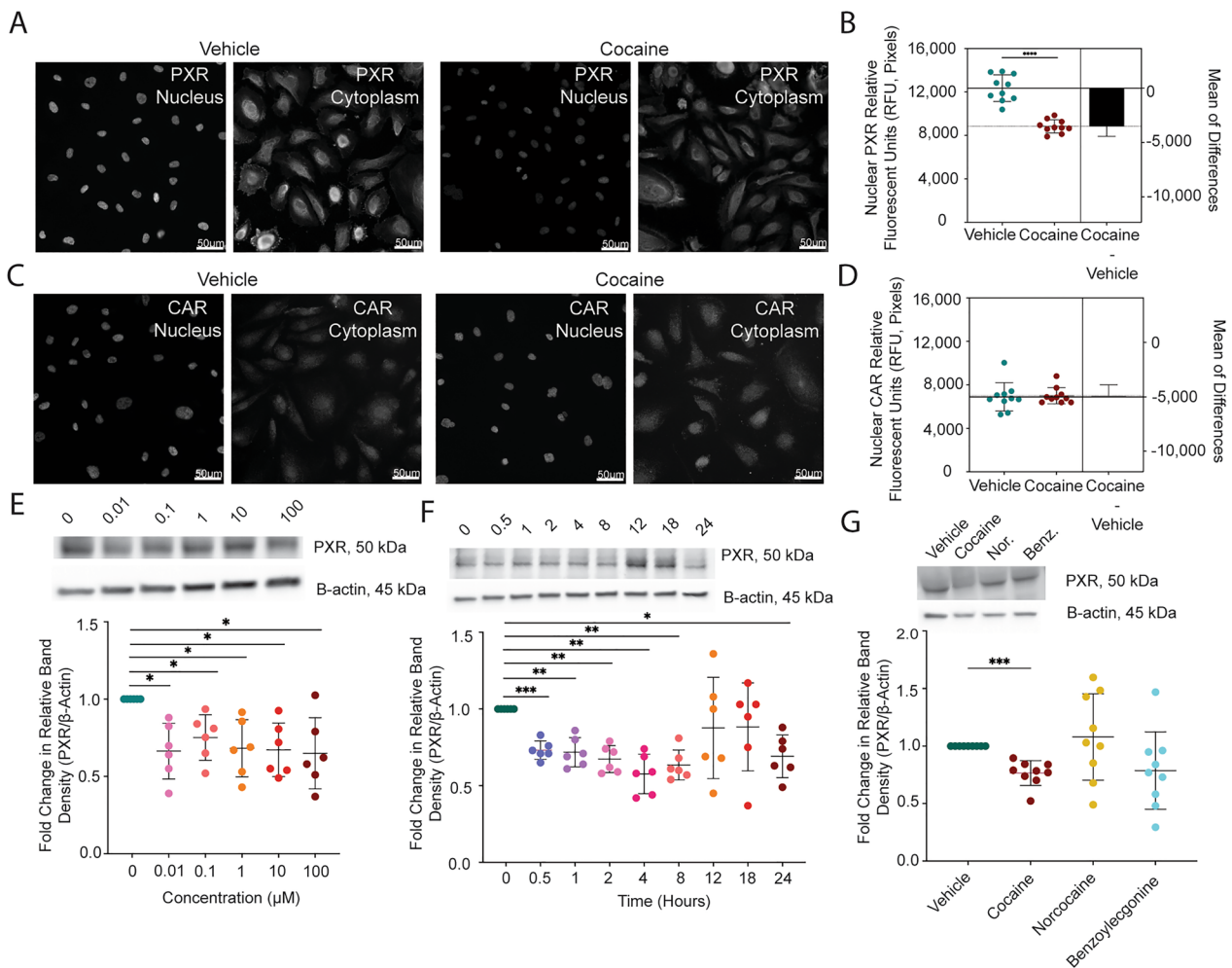


**Fig. 6** Cocaine's Effect on PXR is Specific, Dose-Independent, and Occurs Primarily in the Nucleus. **A–D** Immunofluorescent microscopy was performed to evaluate **A** PXR or **C** CAR following treatment with cocaine (10  $\mu$ M, right) or vehicle (left) for 24 h. The fluorescent signal for each respective protein that colocalized with DAPI was separated from that which occurred in the cytoplasm to facilitate analysis of PXR and CAR specifically in the nucleus. One paired representative image, out of 20 individual images, are shown. All scale bars = 50  $\mu$ m. **(B, D)** Quantification of the nuclear fluorescent signal from **(A)** PXR and **(C)** CAR immunofluorescent microscopy was performed for endothelial cells treated with cocaine (10  $\mu$ M, burgundy) or vehicle (teal) for 24 h. Twenty independent experiments (represented by individual dots) were performed. Estimation plots are shown where the left y-axis denotes relative fluorescent intensity (RFU, pixels) of the nucleus and the right y-axis reflects the effect size (black bar), which is the difference between means of each condition. Data are represented as mean  $\pm$  standard deviation. \*\*\*\*p < 0.0001. Unpaired T-test was performed. **(E)** Western blot was performed to evaluate PXR following 24-h treatment with cocaine (0.01–100  $\mu$ M) or vehicle (0  $\mu$ M).  $\beta$ -actin was used for protein normalization. One western blot, representative of six independent experiments, is shown (top). The fold change in relative band intensity for PXR/ $\beta$ -actin was determined by densitometry where vehicle treatment was set to 1. Six independent experiments (represented by individual dots) were performed. The fold change in relative band intensity for PXR relative to  $\beta$ -actin is depicted (bottom). Data are represented as mean  $\pm$  standard deviation. \*p < 0.05. One-way ANOVA was performed. **F** Western blot was performed to evaluate PXR following 0.5–24 h treatment with cocaine (10  $\mu$ M) or vehicle (0  $\mu$ M).  $\beta$ -actin was used for protein normalization. One western blot, representative of six independent experiments, is shown (top). The fold change in relative band intensity for PXR/ $\beta$ -actin was determined by densitometry where vehicle treatment was set to 1. Six independent experiments (represented by individual dots) were performed. The fold change in relative band intensity for PXR relative to  $\beta$ -actin is depicted (bottom). Data are represented as mean  $\pm$  standard deviation. \*p < 0.05. \*\*p < 0.01. \*\*\*p < 0.001. One-way ANOVA was performed. **(G)** Western blot was performed to evaluate PXR following 24-h treatment with cocaine (10  $\mu$ M), its minor metabolite norcocaine (10  $\mu$ M), its major metabolite benzoylecgonine (10  $\mu$ M) or vehicle.  $\beta$ -actin was used for protein normalization. One western blot, representative of 9 independent experiments, is shown (top). The fold change in relative band intensity for PXR/ $\beta$ -actin was determined by densitometry where vehicle treatment was set to 1. Nine independent experiments (represented by individual dots) were performed. The fold change in relative band intensity for PXR relative to  $\beta$ -actin is depicted following cocaine (burgundy), norcocaine (yellow), benzoylecgonine (turquoise), or vehicle (teal) treatment (bottom). Data are represented as mean  $\pm$  standard deviation. \*\*\*p < 0.001. One-way ANOVA was performed

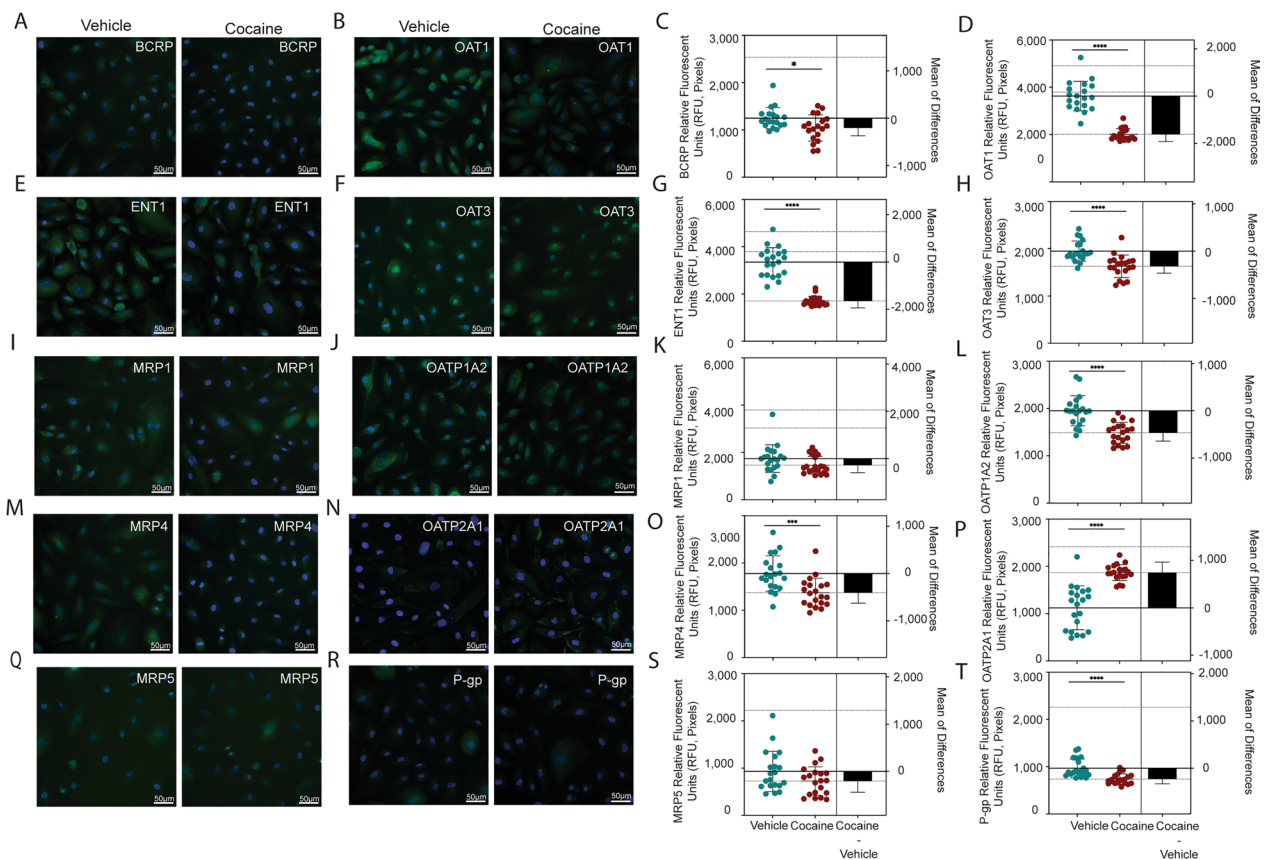


**Fig. 7** Cocaine Modulates Drug Transporter Expression. Immunofluorescent microscopy was performed to evaluate (A) BCRP, (B) OAT1, (E) ENT1, (F) OAT3, (I) MRP1, (J) OATP1A2, (M) MRP4, (N) OATP2A1, (Q) MRP5, or (R) P-gp (green) following treatment with cocaine (10  $\mu$ M, right) or vehicle (left) for 24 h. DAPI was used to visualize nucleus (blue). One paired representative image, out of 20 individual images, are shown. All scale bars = 50  $\mu$ m. (C, D, G, H, K, L, O, P, S, T) Quantification of the fluorescent signal from immunofluorescent microscopy was performed for endothelial cells treated with cocaine (10  $\mu$ M, burgundy) or vehicle (left) for 24 h. Twenty independent experiments (represented by individual dots) were performed. Estimation plots are shown where the left y-axis denotes relative fluorescent intensity (RFU, pixels) and the right y-axis reflects the effect size (black bar), which is the difference between means of each condition. Data are represented as mean  $\pm$  standard deviation. \* $p < 0.05$ . \*\*\* $p < 0.001$ . \*\*\*\* $p < 0.0001$ . Unpaired T-test was performed

cells for 24 h with cocaine, a specific inhibitor for each transporter, or the specific PXR inhibitor resveratrol. Specifically, we used the BCRP inhibitor fumitremorgin (10  $\mu$ M), the MRP4 inhibitor ceefourin 1 (10  $\mu$ M), and P-gp inhibitor ritonavir (10  $\mu$ M). Following treatment, the cells were loaded with a fluorescent dye (Hoechst 33342 for BCRP, monobromobimane for MRP4, and rhodamine 123 for P-gp) whose efflux is known to be mediated by our proteins of interest and compared the remaining intracellular fluorescence in the presence and absence of cocaine and the inhibitors. We determined that cocaine inhibited the efflux activity of all three transporters, indicated by increased intracellular fluorescence (Fig. 8). Each fluorescent dye rapidly entered the cell and was effluxed out after four hours, denoted by the loss of fluorescence when comparing Hoechst 33342 (Fig. 8A), monobromobimane (Fig. 8B), and rhodamine 123 (Fig. 8C) to the vehicle condition. However, cocaine

restored the fluorescent signal of all three dyes, indicating an inhibition of efflux out of the cell. Cocaine had a 39% increase ( $p = 0.0162$ , T-test), a 91% increase ( $p = 0.0011$ , T-test), and a 34% increase ( $p = 0.0148$ , T-test) in the mean fluorescence intensity (MFI) attributed to Hoechst 33342, monobromobimane, and rhodamine 123, respectively. Interestingly, this diminished efflux activity mirrored the decreased expression of BCRP, MRP4, and P-gp induced by cocaine (Fig. 7C, O, T). The impact of cocaine on the efflux transporters was comparable to that of their known inhibitors, strengthening the implications of cocaine in modulating the functional capacity of each transporter. Furthermore, resveratrol had a comparable inhibition on efflux activity as cocaine, demonstrating the importance of PXR in modulating transporter activity. These findings indicate that cocaine modulates transporter activity and identifies PXR as an important mechanism by which it alters the CNS efficacy of ART.

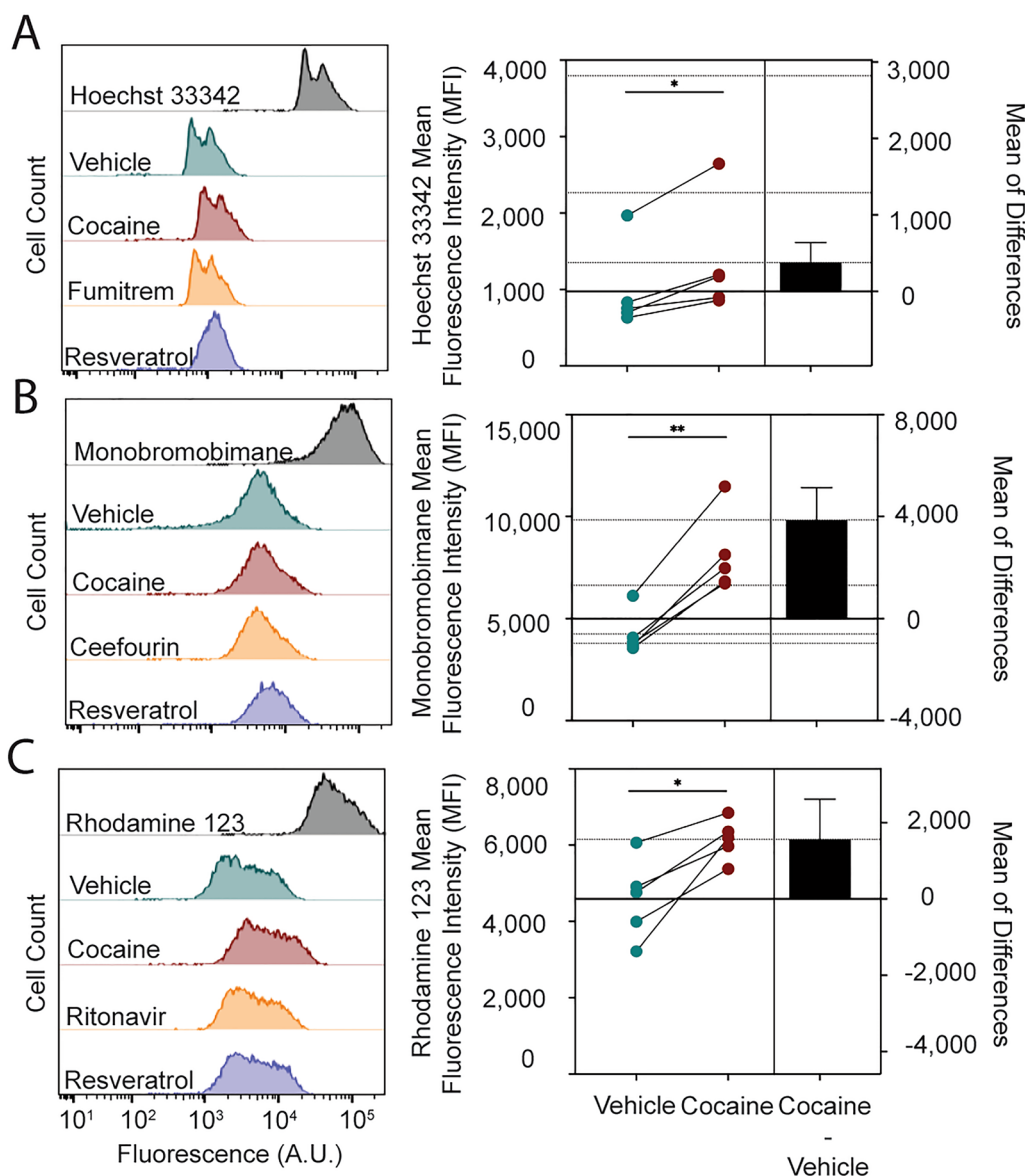


**Fig. 8** Cocaine Decreases BCRP, MRP4, and P-gp Transport Activity. Endothelial cells were loaded with dyes specific for **A** BCRP (Hoechst 33,342, 5 µg/mL), **B** MRP4 (monobromobimane, 10 µM), and **C** P-gp (rhodamine 123, 10 µM) for 1 h (grey) and the dyes allowed to efflux out of the cell for four hours following pre-treatment with cocaine (10 µM, burgundy) or vehicle (teal). The cells were also pre-treated with specific inhibitors of (A) BCRP (10 µM, fumitremorgin), **B** MRP4 (10 µM, ceefourin 1), **C** P-gp (10 µM, ritonavir) (yellow) or PXR (resveratrol, 10 µM, lavender). Flow cytometric analysis was performed to evaluate the fluorescence and one histogram, representative of five independent experiments is shown (left). The fluorescent signal from flow cytometry was determined for endothelial cells pre-treated with cocaine (10 µM, burgundy) or vehicle (teal). Five independent experiments (represented by individual dots) were performed. Estimation plots are shown where the left y-axis denotes the mean fluorescent intensity (MFI, pixels) for **A** Hoechst 33,342 **B** monobromobimane, and **C** rhodamine 123 and the right y-axis reflects the effect size (black bar), which is the difference between means of each condition (right). Data are represented as mean ± standard deviation. \*p < 0.05. \*\*p < 0.01. Paired T-test was performed

**Cocaine regulates enzymes involved in ART metabolism and biotransformation**

In addition to its role in drug transport, PXR also contributes to drug metabolism by regulating phase I oxidative enzymes and phase II enzymes involved in

glucuronic acid conjugation. CYP3A4 is one of the phase I enzymes of relevance for HIV treatment that is present at the BBB and may influence CNS ART availability. Of relevance for this study, CYP3A4 facilitates DTG metabolism into metabolite 3 [130], which was of

interest as we were unable to quantify DTG's ability to cross the BBB. Thus, we evaluated the impact of cocaine on CYP3A4 expression in endothelial cells following 24-h treatment through Western Blot and immunofluorescent microscopy. Cocaine decreased the total protein levels of CYP3A4 as there was a 21% decrease ( $p < 0.0001$ , T-test) in its relative band intensity, as compared to vehicle (Fig. 9A-B). This was confirmed microscopically where cocaine decreased the CYP3A4 RFU, relative to vehicle, by 23% (Fig. 9C-D,  $p = 0.0035$ , T-test). Next, we evaluated the functional consequences of decreased CYP3A4 by evaluating its metabolic activity. Endothelial cells were pre-treated with cocaine or vehicle for 24 h, loaded with the fluorogenic CYP3A4 substrate, BFC [131–133], and fluorescent signal measured over 80 min to evaluate formation of the fluorescent product, HFC. Cells were also pre-treated with rifampicin, as a positive control, and the PXR inhibitor resveratrol.

The rate of HFC production, indicated by fluorescent signal, occurred rapidly in the first 20 min after which time it began to plateau and eventually decline (Additional file 1: Figure S4). We used the linear portion of the curve in this first 20 min (Fig. 9E) to evaluate the rate at which CYP3A4 converted BFC to HFC, termed CYP3A4 velocity. Cocaine increased the CYP3A4 velocity by 273% ( $p = 0.0112$ , one-way ANOVA), as compared to vehicle, from  $545 \pm 372$  RFU/minute to  $1,490 \pm 965$  RFU/minute (Fig. 9F). This effect of cocaine was comparable to that of rifampicin, a well-known and clinically relevant CYP3A4 inducer, which increased the CYP3A4 velocity by 374% ( $p = 0.0001$ , one-way ANOVA) to  $2,039 \pm 1,125$  RFU/minute. Of importance, resveratrol had the most profound effect on CYP3A4 by increasing its velocity by 585% to  $3,188 \pm 1,613$  RFU/minute, confirming the importance of PXR in CYP3A4 regulation (Fig. 9F).

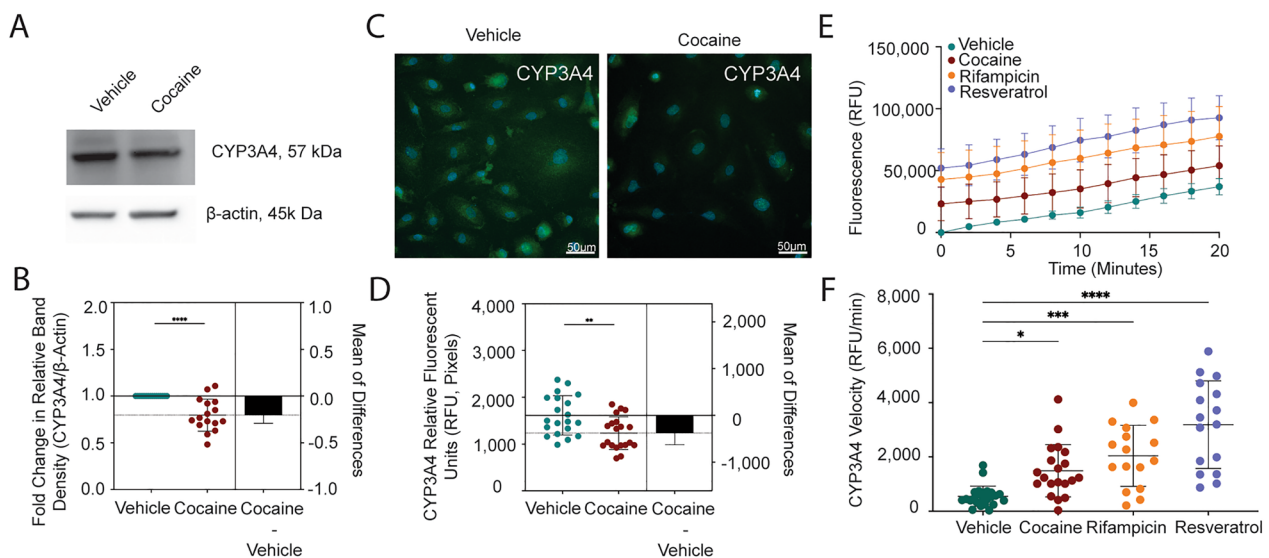


**Fig. 9** Cocaine Decreases CYP3A4 to Compensate for Increased Enzymatic Activity. **A** Western blot was performed to evaluate CYP3A4 following 24-h treatment with cocaine (10  $\mu$ M) or vehicle.  $\beta$ -actin was used for protein normalization. One western blot, representative of 16 independent experiments, is shown. **B** The fold change in relative band intensity for CYP3A4/ $\beta$ -actin was determined by densitometry where vehicle treatment was set to 1. Sixteen independent experiments (represented by individual dots) were performed. The fold change in relative band intensity for CYP3A4 relative to  $\beta$ -actin is depicted (bottom). Data are represented as mean  $\pm$  standard deviation. \* $p < 0.05$ . One-way ANOVA was performed. **C** Immunofluorescent microscopy was performed to evaluate CYP3A4 (green) following treatment with cocaine (10  $\mu$ M, right) or vehicle (left) for 24 h. DAPI was used to visualize the nucleus (blue). One paired representative image, out of 20 individual images, is shown. All scale bars = 50  $\mu$ m. **D** Quantification of the fluorescent signal from CYP3A4 immunofluorescent microscopy was performed for endothelial cells treated with cocaine (10  $\mu$ M, burgundy) or vehicle (teal) for 24 h. Twenty independent experiments (represented by individual dots) were performed. Estimation plots are shown where the left y-axis denotes relative fluorescent intensity (RFU, pixels) and the right y-axis reflects the effect size (black bar), which is the difference between means of each condition. Data are represented as mean  $\pm$  standard deviation. \*\* $p < 0.01$ . Unpaired T-test was performed. **E** Endothelial cells were pre-treated with cocaine (10  $\mu$ M, burgundy), rifampicin (1  $\mu$ M, yellow), resveratrol (10  $\mu$ M, lavender), or vehicle (teal) for 24 h, after which time the cells were loaded with BFC (2  $\mu$ M). The enzymatic capacity of CYP3A4 to convert BFC to HFC was determined for the first 20 min as determined by fluorometric quantitation at excitation and emission wavelengths of 405/535 nm. Twelve independent experiments that contained eight technical replicates per condition were performed. Data are represented as mean  $\pm$  standard deviation. \*\* $p < 0.01$ . \*\*\*\* $p < 0.0001$ . Unpaired T-test was performed. **F** The rate at which BFC was converted to HFC is depicted as CYP3A4 velocity (RFU/min) for the earliest time points (2 and 4 min) to evaluate maximal enzymatic activity. The CYP3A4 velocity for each time point was pooled for both time points. Twelve independent experiments for each time point (represented by combined 24 individual dots) were performed. Data are represented as mean  $\pm$  standard deviation. \* $p < 0.05$ . \*\*\* $p < 0.001$ . \*\*\*\* $p < 0.0001$ . One-way ANOVA was performed

We also wanted to evaluate the effect of cocaine on the metabolism of TFV and FTC, which are not CYP3A4 substrates. TFV and FTC are given as prodrugs that require biotransformation through a series of phosphorylation events to become pharmacologically capable of inhibiting HIV reverse transcriptase. Endogenous kinases, including adenylate kinases, are used to accomplish these phosphorylation events. Of the nine adenylate kinase isoforms, we evaluated AK1, AK2, and AK6 as they are the only isoforms that can use all ribonucleoside triphosphates as phosphate donors, as well as AK5 because it is exclusively expressed in the brain. Endothelial cells were treated with cocaine or vehicle for 24 h and adenylate kinase expression was evaluated by immunofluorescent microscopy. Cocaine modulated AK1, AK5, and AK6, but not AK2, by causing a 20% increase ( $p=0.0012$ , T-test), a 13% decrease ( $p=0.0334$ , T-test), and a 19% increase ( $p=0.0011$ , T-test), in the RFU as compared to vehicle, respectively (Additional file 1: Figure S5). Collectively, these findings demonstrate the implications of cocaine and PXR in altering ART metabolism that can impact its availability in the brain and ability to be efficacious in suppressing HIV.

## Discussion

In this study, we demonstrated that cocaine modulates ART availability in the brain through regulation of drug transport and metabolism pathways at the BBB. Unexpectedly, we determined that cocaine did not perturb BBB integrity, but rather, downregulated PXR – the master regulator of drug transport and metabolism – to mediate its effects. Of importance, the impact of cocaine on ART extravasation across the BBB was not uniform, but instead, varied by drug. Our findings have profound implications for treatment of people with HIV with comorbid cocaine use disorders. Further, this work raises additional concerns for all substance using populations, not only those living with HIV, as the PXR-mediated drug transport and metabolism pathways explored in our present work are implicated in facilitating CNS access for therapeutics that treat essentially every neurologic disease.

The brain represents a major HIV reservoir. As such, the CNS efficacy of ART is a substantial barrier to HIV eradication efforts and remains a focus of much scientific and clinical investigation. Efforts to understand ART availability in the brain were once limited to predictive analyses based on chemical properties of individual drugs and their cerebrospinal fluid concentrations [111, 134–136]. However, more recent evidence obtained from sampling distinct brain regions demonstrates that unexpectedly higher ART levels reach the CNS than previously considered [7, 100–111, 137–139]. Even still, these

concentrations are not comparable to those present in peripheral organs and people with HIV continue to have neurologic complications despite having undetectable plasma viral loads. Together, these concerns highlight the importance of understanding the molecular mechanisms by which ART traverses the BBB. Currently, our knowledge is limited and restricted to extrapolation from studies in peripheral organs – namely liver and small intestine. From these important studies we understand the transporters and metabolic enzymes capable of interacting with ART, including CYP3A4, P-gp, BCRP, and MRP4, as well as the importance of key transcriptional regulators PXR and CAR. As these proteins are also present and functional at the BBB, we assume that these same processes are involved in facilitating ART extravasation into the brain. However, studies demonstrating this are lacking. Our study addresses this gap in knowledge by demonstrating the importance of PXR in regulating drug transporter and metabolizing enzyme activity at the BBB.

Substance use is an important contributor to CNS HIV disease as it modulates neuroinflammatory, oxidative stress, and energy metabolic pathways [60, 62, 64, 65, 140–145]. Additionally, there is a strong premise that substance use adversely impacts the BBB [61, 66, 67, 146–157]. Most studies focused primarily on BBB integrity, transendothelial electrical resistance, and permeability. However, to our knowledge, there have been no studies evaluating the impact of substance use on ART's ability to traverse the BBB into the CNS compartment. For these reasons, we sought to evaluate the impact of substance use on this important, but understudied, aspect that perpetuates HIV CNS disease using cocaine as a model illicit substance. We determined that cocaine increased FTC's ability to cross the BBB, while decreasing that of TFV. This was intriguing because cocaine reversed their inherent differential ability to penetrate the BBB. Cocaine's opposing effect on the ability of FTC and TFV to cross the BBB is quite striking, and concerning, as they are remarkably similar: they belong to the same ART class and have comparable molecular weights, structures, biophysical properties, pharmacokinetic distribution properties, substrate specificity, and phosphorylation-dependency to become pharmacologically capable of inhibiting HIV. This suggests that *in silico* and other predictive modeling analyses would be ineffective at predicting the differential impact of cocaine on ART availability in brain, which could have devastating clinical consequences. Our findings are an initial attempt at evaluating the impact of substance use on ART entry to the CNS and demonstrates that additional studies are warranted that consider the remaining ART drugs, as well as other substances of abuse. Furthermore, our

findings provide caution to people without HIV who are prescribed these medications for pre-exposure prophylaxis (PrEP), as FTC and either the disoproxil fumarate or alafenamide formulations of TFV are co-administered in Truvada<sup>®</sup> and Descovy<sup>®</sup>, respectively, the FDA approved drugs for HIV prevention [158–161]. Indeed, care must be taken as our study raises the concern that cocaine use, and potentially other substances of abuse as well, while taking PrEP may alter its bioavailability and potential to prevent HIV transmission.

We were surprised to determine that cocaine didn't adversely impact BBB integrity or permeability as it contrasts with the general consensus in the field. We posit that experimental differences in study design contribute to our discrepant finding, including species of origin, BBB model, and the tracers used to evaluate permeability. While unexpected, our analyses included measures of albumin and 4 kDa FITC-dextran permeability, tight junction and adhesion molecule expression, and evaluation of the entire proteomic landscape. Indeed, we employed qRT-PCR, Western blot, flow cytometry, and mass spectrometry to evaluate multiple aspects that help maintain BBB integrity. Thus, while unexpected, our complimentary methodologies are rigorous and demonstrate that cocaine's impact on ART extravasation occurred by additional mechanisms. Our work provides evidence of the importance of evaluating BBB function beyond integrity and permeability measures by including functional analyses, such as drug extravasation studies. Further, it urges investigators to evaluate critically seemingly discrepant results if their disease model of interest does not perturb the BBB, as other underappreciated mechanisms may be involved. It is our hope that our findings expand the scope of considerations for how illicit substances, and other disease settings, impact BBB function.

Cocaine's functional capacity to impact BBB transport pathways is of major interest in HIV CNS treatment strategies. The brain is notoriously difficult to treat as ~98% of all small molecule therapeutics fail to penetrate the BBB [162–166]. As a result, understanding the mechanisms by which therapeutics and illicit substances alter influx and efflux transport mechanisms is critical for effective treatment plans. We found that cocaine modulated eight transporters, where primarily decreased expression occurred (7/8 transporters). Five of these transporters facilitate influx into the brain, while the remainder are involved in efflux. Not only were the expression levels of the proteins affected, but cocaine also decreased their functional capacity to transport well-characterized substrates. Importantly, inhibiting PXR with resveratrol promoted an effect comparable to cocaine, further implicating the transcription factor as an important

transport regulatory mechanism. These findings suggest that cocaine inhibits the potential of ART, and possibly other therapeutics as well, from entering the brain due to decreased influx transporter expression and activity. However, our work also indicates that cocaine also stabilizes CNS concentrations by preventing efflux out of the brain. These competing mechanisms provide insight regarding why cocaine may have distinct effects on the CNS concentrations of differing ART drugs. The cocaine-induced changes in drug transporter and metabolizing enzyme expression and function may have a direct contribution to the observed alterations in TFV and FTC BBB extravasation. The transporters and drug metabolizing enzymes evaluated in our study are all implicated in interacting with TFV, FTC, and ART more broadly, which is why they were the focus of our study. As such, they are widely accepted as the presumed major players involved in ART disposition [16, 19]. However, as we determined cocaine regulated multiple transporters and drug metabolizing enzymes, it is unclear how these competing mechanisms are simultaneously regulated by PXR and what the implications are for ART CNS disposition.

To our knowledge, this is the first time cocaine is implicated in modulating these transport processes. However, it should be noted that cocaine's effect on drug transport shouldn't be all that surprising, as it is classically known to mediate its rewarding effects by inhibiting dopamine, norepinephrine, and serotonin transporters [167–179]. Further, there is increasing evidence that cocaine may impact other transporters, including those involved in glymphatic CNS clearance mechanisms [180]. Interestingly, other addictive substances, including nicotine, opioids, and ethanol, affect transporter activity suggesting an overarching mechanism by which substance use may contribute to drug:drug interactions that adversely impact treatment strategies [181–187]. Our findings posit that further investigation regarding the mechanisms by which cocaine, and other illicit substances, modulate CNS transport mechanisms more broadly are warranted, as they are integral in maintaining the specialized microenvironment of the brain that also have implications for therapeutic efforts.

We identified drug metabolism and biotransformation as additional mechanisms by which cocaine regulates the ability of ART to cross the BBB. Initially, we focused on CYP3A4 to provide insight into cocaine's impact on DTG CNS concentrations, as we were unable to quantify its BBB transport. However, our findings have much broader implications as CYP3A4 is involved in metabolism of many ART drugs, including reverse transcriptase inhibitors, protease inhibitors, entry inhibitors, and other integrase inhibitors. Our findings demonstrate that cocaine decreases CYP3A4 expression by a

PXR-mediated mechanism. Interestingly, this decrease in expression contributes to increased CYP3A4 enzymatic activity, as measured by HFC production. These findings suggest a compensatory mechanism by which PXR decreases CYP3A4 at the protein level to accommodate for its increased enzymatic efficiency. This impact of cocaine on CYP3A4 activity is remarkable as it is comparable to that of the well-known and clinically relevant CYP3A4 inducer, rifampicin. These findings have substantial clinical implications as CYP3A4 is the most abundant human cytochrome p450 isoform. Additionally, CYP3A4 is involved in the metabolism of 60% of all prescribed therapies. Our work identifies cocaine as a major modulator of CYP3A4, comparable to rifampicin, that has the potential to alter pharmacokinetics and dosing strategies for ART and other therapeutic drugs – including those that act in peripheral organs. This is the first time, to our knowledge, cocaine has been identified to regulate CYP3A4 enzymatic activity. Interestingly, other illicit substances also modulate CYP3A4 and other cytochrome P450's [181–187]. Furthermore, substance use can impact plasma concentrations of ART and viral rebound, independent of adherence concerns [188–190]. Together, our findings demonstrate that additional attention is warranted in the clinical care of substance using populations with HIV, where measures of viral suppression and plasma ART concentrations are evaluated more regularly to evaluate treatment efficacy.

In addition to CYP3A4, we determined that cocaine also regulated the adenylate kinases involved in biotransformation of ART prodrugs into their pharmacologically active counterparts capable of suppressing HIV. Specifically, cocaine increased AK1, AK5, and AK6, but not AK2, demonstrating selectivity in its effects. As AK1 is ubiquitously expressed, our findings suggest cocaine's impact on ART biotransformation may occur throughout the body, including the immune cells that are the primary target for HIV. Our findings also demonstrate a mechanism by which cocaine may specifically regulate ART CNS concentrations through modulation of the brain-specific AK5 isoform. This suggests a unique role for cocaine in regulating the ability of ART to be efficacious specifically in the CNS reservoir, primarily microglia, macrophages, and potentially astrocytes as their infection is a point of much discussion in the field.

## Conclusions

Our findings identify cocaine as an important contributor to the CNS efficacy of ART by altering its ability to cross the BBB and regulating PXR-mediated drug transport and metabolism pathways. Contrary to convention, cocaine's effects did not breach BBB integrity, as evidenced by targeted evaluation of key proteins involved

in barrier integrity, global proteomic evaluation, and permeability measures. Further, cocaine increased FTC's ability to cross the BBB while decreasing that of TFV, providing additional evidence of regulated, nuanced, and selective mechanisms rather than general loss of permeability. For the first time, we introduce awareness of the clinical ramifications of comorbid substance use in HIV cure strategies, specifically for viral eradication strategies in the brain. Furthermore, our findings provide insight into cocaine's impacts on therapeutic strategies beyond HIV treatment, as PXR's regulation of P-gp, BCRP, MRP4, and CYP3A4 activity are involved in drug disposition for numerous disorders.

## Abbreviations

TBS-T	1X Tris-Buffered Saline containing 0.1% Tween-20
BFC	7-Benzoyloxy-4-trifluoromethylcoumarin
HFC	7-Hydroxy-4-trifluoromethylcoumarin
ABC	ATP-binding cassette
ART	Antiretroviral therapy
AIDS	Acquired immunodeficiency syndrome
ALCAM	Activated leukocyte cell adhesion molecule
BBB	Blood brain barrier
BCRP	Breast Cancer Resistant Protein
CTSB	Cathepsin B
CNS	Central nervous system
COL6A1	Collagen Type VI Alpha 1 Chain
cART	Combined ART
M199C	Complete M199 media
DPBS	Dulbecco's phosphate-buffered saline without calcium or magnesium
DTG	Dolutegravir
EDTA	Ethylenediaminetetraacetic acid
FTC	Emtricitabine
ENT	Equilibrative nucleoside transporter
Evans	Blue dye conjugated to albumin
FBS	Fetal bovine serum
GM-CSF	Granulocyte-macrophage colony-stimulating factor
HPX	Hemopexin
HIV	Human immunodeficiency virus-1
ICAM-1	Intercellular Adhesion Molecule 1
IFN- $\alpha$ 2	Interferon $\alpha$ 2
IFN- $\beta$	Interferon $\beta$
IFN- $\gamma$	Interferon $\gamma$
IP-10	Interferon $\gamma$ -inducible protein 10 kD
IFN- $\lambda$ 1	Interferon $\lambda$ 1
IFN- $\lambda$ 2/3	Interferon $\lambda$ 2/3
IL-10	Interleukin 10
IL-12p70	Interleukin 12p70
IL-1 $\beta$	Interleukin 1 $\beta$
IL-6	Interleukin 6
IL-8	Interleukin 8
JAM-A	Junctional adhesion molecule A
LPS	Lipopolysaccharide
MIF	Macrophage Migration Inhibitory Factor P
MFI	Mean fluorescence intensity
M199	Medium 199
MRP4	Multidrug resistance-associated protein 1
MRP2	Multidrug resistance-associated protein 2
MRP4	Multidrug resistance-associated protein 4
NRP2	Neuropilin 2
OAT1	Organic anion transporter 1
OAT3	Organic anion transporter 3
OATP1A2	Organic anion-transporting polypeptide 1A2
OD <sub>620</sub>	Optical density at 620 nm

PECAM-1	Platelet-endothelial cell adhesion molecule
P-gp	P-glycoprotein
PBS	Phosphate buffered saline
ICALM	Phosphatidylinositol Binding Clathrin Assembly Protein
PrEP	Pre-exposure prophylaxis
PXR	Pregnane-X receptor
ROI	Region of interest
RFU	Relative fluorescent intensity
SLC	Solute carrier transporter
TFV	Tenofovir
TNF- $\alpha$	Tumor necrosis factor alpha
VTN	Vitronectin
VWF	Von Willebrand Factor
Zo-1	Zonula occludens-1

## Supplementary Information

The online version contains supplementary material available at <https://doi.org/10.1186/s12987-023-00507-3>.

**Additional file 1: Figure S1.** Brain Microvascular Endothelial Cells and Astrocytes Express Characteristic Markers. Immunofluorescent microscopy was performed to evaluate expression of anticipated markers in (A-G) primary human brain microvascular endothelial cells and (H) primary human astrocytes. (Left panels) Antibodies with specificity to (A) CD71, (B) claudin-5, (C) GLUT-1, (D) VE-Cadherin, (E) occludin, (F) PECAM-1, (G) Zo-1, and (H) GFAP were coupled to Alexa Fluor 488 for analysis. (Middle panels) DAPI was used to visualize nucleus. (Right panels) Merge depicts the combined signal for proteins of interest (green) and DAPI (blue). Representative images, out of 20 independent images, are shown. All scale bars = 50  $\mu$ m. **Figure S2.** In vitro Model of the Human BBB. (A) Schematic representation of our transwell BBB model where primary human brain microvascular endothelial cells are seeded on the upper, apical compartment and primary human astrocytes are seeded on the underside of a polycarbonate membrane with 3  $\mu$ m pores in the basolateral compartment. (B) Schematic representation of albumin permeability assay, where EBA dye is added to the apical portion and permitted to pass to the basolateral side for 30 min at 37  $^{\circ}$ C, 5% CO<sub>2</sub>. The media in the basolateral side is collected and spectrophotometrically read at OD<sub>620</sub> to evaluate BBB permeability. (C-F) The polycarbonate membrane from the BBB model was collected, immunostained, and immunofluorescent microscopy performed. (C-D) Wheat germ agglutinin (WGA) depicts cell morphology in red and (E-F) demonstrates expression of the astrocyte and endothelial cell markers GFAP and VE-Cadherin, respectively in green. DAPI was used to visualize nucleus (blue). Representative images, out of 3–5 independent images, are shown. All scale bars = 50  $\mu$ m. **Figure S3.** Cocaine and LPS Do Not Promote Loss of Endothelial Cell Viability. Endothelial cells were treated with cocaine (10  $\mu$ M, burgundy), LPS (10 ng/mL, fuschia), or vehicle (teal) for (A) 0.5 or (B) 24 h, after which time the cells were loaded with the BD Horizon Fixable Viability Stain 520 for 15 min at 37  $^{\circ}$ C, 5% CO<sub>2</sub>. Following treatment, the cells were acquired on the BD LSRFortessa cytometer and Diva software version 9 on the Windows 10 platform (BD Biosciences). Flow cytometric data were analyzed using FlowJo version 10.9 (FlowJo, Ashland, OR). **Figure S4.** Complete Duration of CYP3A4 Metabolic Activity Assay. Endothelial cells were pre-treated with cocaine (10  $\mu$ M, burgundy), rifampicin (1  $\mu$ M, yellow), resveratrol (10  $\mu$ M, lavender), or vehicle (teal) for 24 h, after which time the cells were loaded with BFC (2  $\mu$ M). The enzymatic capacity of CYP3A4 to convert BFC to HFC was determined for 80 min as determined by fluorometric quantitation at excitation and emission wavelengths of 405/535 nm. Twelve independent experiments that contained eight technical replicates per condition were performed. Data are represented as mean  $\pm$  standard deviation. **Figure S5.** Cocaine Modulates AK1, AK5, and AK6 Expression. Immunofluorescent microscopy was performed to evaluate (A) AK1, (B) AK2, (C) AK5, and (G) AK6 (green) following treatment with cocaine (10  $\mu$ M, right) or vehicle (left) for 24 h. DAPI was used to visualize nucleus (blue). One paired representative image, out of 20 individual images, are shown. All scale bars = 50  $\mu$ m. Quantification of the fluorescent signal from immunofluorescent microscopy was performed for endothelial cells treated with cocaine (10  $\mu$ M, burgundy) or vehicle (teal) for 24 h. Twenty independent

experiments (represented by individual dots) were performed. Estimation plots are shown where the left y-axis denotes relative fluorescent intensity (RFU, pixels) and the right y-axis reflects the effect size (black bar), which is the difference between means of each condition. Data are represented as mean  $\pm$  standard deviation. \* $p$  < 0.05. \*\* $p$  < 0.01. Unpaired T-test was performed.

## Acknowledgements

We thank Mr. Mark Marzinke of the Clinical Pharmacology Analytical Lab for his assistance with antiretroviral therapy determination. We acknowledge and thank the NIDA Drug Supply Program for providing the cocaine hydrochloride used in this study. We thank the members of the Johns Hopkins School of Medicine Retrovirus Laboratory in the Department of Molecular and Comparative Pathobiology for their support. Images in figures were created using Biorender.

## Author contributions

RCO, SK, LBF, AM, ASP, JJRF, HW, BRF, and DWW performed experiments. LBF, SK, ASP, RCC, HW, BCO, and DWW analyzed data. DWW was responsible for conceptualization of the study design. DWW wrote the original draft of the manuscript with review and editing from all authors. All authors read and approved the final manuscript.

## Funding

Research reported in this publication was supported by the National Institutes of Health under award number R00 DA044838 (DWW), R01 DA052859 (DWW), and U01 DA058527 (DWW), R01 GM103853 (BCO), and R01 AG064908 (BCO). Additionally, HNW was supported by T32 GM144272 granted to the Biochemistry, Cellular & Molecular Biology Graduate Program at Johns Hopkins and AM was supported by R25 GM109441 granted to the Post-baccalaureate Research Education Program at Johns Hopkins. This work was supported, in part, by pilot funding provided by parent funding under the JHU NIMH Center for Novel Therapeutics for HIV-associated Cognitive Disorders P30 MH075673 to Justin C. McArthur. The authors also acknowledge mentorship to DWW from the Johns Hopkins University Center for AIDS Research (P30 AI094189). The content is solely the responsibility of the authors and does not necessarily represent the official views of the National Institutes of Health.

## Availability of data and materials

All data generated or analyzed during this study are included in this published article and are available from the corresponding author on reasonable request. All vendor original LCMS data and processed data has been made publicly available through the ProteomeXchange and MASSIVE public repositories<sup>191</sup>. Data can be directly accessed through FTP at the following link: <ftp://MSV000092529@massive.ucsd.edu>.

## Declarations

### Ethics approval and consent to participate

Not applicable.

### Consent for publication

Not applicable.

### Competing interests

The authors declare that they have no competing interests.

### Author details

<sup>1</sup>Department of Neuroscience, Johns Hopkins School of Medicine, Baltimore, MD 21205, USA. <sup>2</sup>Department of Molecular and Comparative Pathobiology, Johns Hopkins School of Medicine, Baltimore, MD 21205, USA. <sup>3</sup>Department of Pharmacology and Molecular Sciences, Johns Hopkins School of Medicine, Baltimore, MD 21205, USA. <sup>4</sup>Department of Medicine, Division of Clinical Pharmacology, Johns Hopkins School of Medicine, Baltimore, MD 21205, USA. <sup>5</sup>Department of Molecular Microbiology & Immunology, Johns Hopkins School of Public Health, Baltimore, MD 21205, USA. <sup>6</sup>Department of Pharmacology and Chemical Biology, Emory University School of Medicine, Rollins Research Center, 1510 Clifton Road NE, 30322 Atlanta, Georgia.

Received: 29 July 2023 Accepted: 28 December 2023  
Published online: 10 January 2024

## References

- Davenport MP, et al. Functional cure of HIV: the scale of the challenge. *Nat Rev Immunol*. 2019;19:45–54.
- Palmisano L, Vella S. A brief history of antiretroviral therapy of HIV infection: success and challenges. *Ann dell'Ist Super di Sanita*. 2011;47:44–8.
- Velasco-Hernandez J, Gershengorn H, Blower S. Could widespread use of combination antiretroviral therapy eradicate HIV epidemics? *Lancet Infect Dis*. 2002;2:487–93.
- Shen L, Siliciano RF. Viral reservoirs, residual viremia, and the potential of highly active antiretroviral therapy to eradicate HIV infection. *J Allergy Clin Immunol*. 2008;122:22–8.
- Rudd H, Toborek M. Pitfalls of antiretroviral therapy: current status and long-term CNS toxicity. *Biomol*. 2022;12:894.
- Brew BJ, et al. HIV eradication symposium: will the brain be left behind? *J Neurovirol*. 2015;21:322–34.
- Nicol MR, McRae M. Treating viruses in the brain: perspectives from NeuroAIDS. *Neurosci Lett*. 2021. <https://doi.org/10.1016/j.neulet.2021.135691>.
- Stauch KL, Emanuel K, Lamberty BG, Morsey B, Fox HS. Central nervous system-penetrating antiretrovirals impair energetic reserve in striatal nerve terminals. *J Neurovirol*. 2017;23:795–807.
- Ash MK, Al-Harathi L, Schneider JR. HIV in the brain: identifying viral reservoirs and addressing the challenges of an HIV cure. *Nato Adv Sci Inst Se*. 2021;9:867.
- Chaillon A, et al. HIV persists throughout deep tissues with repopulation from multiple anatomical sources. *J Clin Invest*. 2020. <https://doi.org/10.1172/jci134815>.
- Devanathan AS, Kashuba ADM. Human immunodeficiency virus persistence in the spleen: opportunities for pharmacologic intervention. *Aids Res Hum Retrov*. 2021. <https://doi.org/10.1089/aid.2020.0266>.
- Cochrane CR, et al. Intact HIV proviruses persist in the brain despite viral suppression with ART. *Ann Neurol*. 2022;92:532–44.
- Angelovich TA, et al. Regional analysis of intact and defective HIV proviruses in the brain of viremic and virally suppressed people with HIV. 2023. *Ann Neurol*. <https://doi.org/10.1002/ana.26750>.
- Banks WA. From blood–brain barrier to blood–brain interface: new opportunities for CNS drug delivery. *Nat Rev Drug Discov*. 2016;15:275–92.
- Pandit R, Chen L, Götz J. The blood–brain barrier: physiology and strategies for drug delivery. *Adv Drug Deliv Rev*. 2020;165:1–14.
- Whyte-Allman S-K, Bendayan R. HIV-1 sanctuary sites—the role of membrane-associated drug transporters and drug metabolic enzymes. *AAPS J*. 2020;22:118.
- Whyte-Allman S-K, et al. Drug efflux transporters and metabolic enzymes in human circulating and testicular T-cell subsets: relevance to HIV pharmacotherapy. *AIDS*. 2020;34:1439–49.
- Alam C, Whyte-Allman S-K, Omeragic A, Bendayan R. Role and modulation of drug transporters in HIV-1 therapy. *Adv Drug Deliver Rev*. 2016;103:121–43.
- Kis O, Robillard K, Chan GNY, Bendayan R. The complexities of antiretroviral drug–drug interactions: role of ABC and SLC transporters. *Trends Pharmacol Sci*. 2010;31:22–35.
- Lakhman SS, Ma Q, Morse GD. Pharmacogenomics of CYP3A: considerations for HIV treatment. *Pharmacogenomics*. 2009;10:1323–39.
- Khan MA, Gupta KK, Singh SK. A review on pharmacokinetics properties of antiretroviral drugs to treat HIV-1 infections. *Curr Comput*. 2021;17:850–64.
- Adams JL, Greener BN, Kashuba ADM. Pharmacology of HIV integrase inhibitors. *Curr Opin HIV AIDS*. 2012;7:390–400.
- Panayiotou C, Solaroli N, Karlsson A. The many isoforms of human adenylate kinases. *Int J Biochem Cell Biology*. 2014;49:75–83.
- Tillotson J, Bumpus N. Impact of adenylate kinases and naturally occurring adenylate kinase 2 variants on the phosphorylation of the anti-HIV drug tenofovir. *FASEB J*. 2018. [https://doi.org/10.1096/fasebj.2018.32.1\\_supplement.564.12](https://doi.org/10.1096/fasebj.2018.32.1_supplement.564.12).
- Rompay ARV, Johansson M, Karlsson A. Phosphorylation of nucleosides and nucleoside analogs by mammalian nucleoside monophosphate kinases. *Pharmacol Ther*. 2000;87:189–98.
- Pruvost A, et al. Measurement of intracellular didanosine and tenofovir phosphorylated metabolites and possible interaction of the two drugs in human immunodeficiency virus-infected patients. *Antimicrob Agents Chemother*. 2005;49:1907–14.
- Anderson PL, et al. Pharmacological considerations for tenofovir and emtricitabine to prevent HIV infection. *J Antimicrob Chemother*. 2011;66:240–50.
- Figueroa DB, et al. genetic variation of the kinases that phosphorylate tenofovir and emtricitabine in peripheral blood mononuclear cells. *AIDS Res Hum Retroviruses*. 2018;34:421–9.
- Ouyang B, et al. Simultaneous determination of tenofovir alafenamide and its active metabolites tenofovir and tenofovir diphosphate in HBV-infected hepatocyte with a sensitive LC–MS/MS method. *J Pharm Biomed Anal*. 2017;146:147–53.
- Koch K, et al. Nucleoside diphosphate kinase and the activation of antiviral phosphonate analogs of nucleotides: binding mode and phosphorylation of tenofovir derivatives. *Nucleosides, Nucleotides Nucleic Acids*. 2009;28:776–92.
- Asensi V, Collazos J, Valle-Garay E. Can antiretroviral therapy be tailored to each human immunodeficiency virus-infected individual? Role of pharmacogenomics *World J Virol*. 2015;4:169.
- Dalal B, Shankarkumar A, Ghosh K. Individualization of antiretroviral therapy—Pharmacogenomic aspect. *Indian J Méd Res*. 2015;142:663–74.
- Yu ZJ, Mosher EP, Bumpus NN. Pharmacogenomics of antiretroviral drug metabolism and transport. *Annu Rev Pharmacol Toxicol*. 2020;61:1–21.
- Pavlos R, Phillips EJ. Individualization of antiretroviral therapy. *Pharmacogenomics Pers Med*. 2011;5:1–17.
- Prague M, Commenges D, Thiébaud R. Dynamical models of biomarkers and clinical progression for personalized medicine: the HIV context. *Adv Drug Deliv Rev*. 2013;65:954–65.
- Jensen SO, van Hal SJ. Personalized medicine and infectious disease management. *Trends Microbiol*. 2017;25:875–6.
- Kumbale CM, Voit EO. Toward personalized medicine for HIV/AIDS. *J AIDS HIV Treat*. 2021;3:37–41.
- Edelman EJ, Rentsch CT, Justice AC. Polypharmacy in HIV: recent insights and future directions. *Curr Opin HIV AIDS*. 2020;15:126–33.
- Bositis CM, Louis J. St HIV and substance use disorder role of the HIV physician. *Infect Dis Clin North Am*. 2019;33:835–55.
- Korthuis PT, Edelman EJ. Substance use and the HIV care continuum: important advances. *Addict Sci Clin Pr*. 2018;13:13.
- Leigh BC, Stall R. Substance use and risky sexual behavior for exposure to HIV. *Am Psychol*. 1993;48:1035–45.
- Campbell ANC, Tross S, Calsyn DA. Substance use disorders and HIV/AIDS prevention and treatment intervention: research and practice considerations. *Soc Work Public Heal*. 2013;28:333–48.
- Berg CJ, Michelson SE, Safren SA. Behavioral aspects of HIV care: adherence, depression, substance use, and HIV-transmission behaviors. *Infect Dis Clin North Am*. 2007;21:181–200.
- Hartzler B, et al. Prevalence and predictors of substance use disorders among HIV care enrollees in the United States. *AIDS Behav*. 2017;21:1138–48.
- Millar BM, Starks TJ, Gurung S, Parsons JT. The impact of comorbidities, depression, and substance use problems on quality of life among older adults living with HIV. *AIDS Behav*. 2017;21:1684–90.
- Edelman EJ, Tetraut JM, Fiellin DA. Substance use in older HIV-infected patients. *Curr Opin HIV AIDS*. 2014;9:317–24.
- Carrico AW. Substance use and HIV disease progression in the HAART era: Implications for the primary prevention of HIV. *Life Sci*. 2011;88:940–7.
- Gonzalez A, Barinas J, O'Cleirigh C. Substance use: impact on adherence and HIV medical treatment. *Curr HIV/AIDS Rep*. 2011;8:223.
- White JM, Gordon JR, Mimiaga MJ. The role of substance use and mental health problems in medication adherence among HIV-infected MSM. *LGBT Heal*. 2014;1:319–22.
- Gonzalez A, Mimiaga MJ, Israel J, Bedoya CA, Safren SA. Substance use predictors of poor medication adherence: the role of substance use

- coping among HIV-infected patients in opioid dependence treatment. *AIDS Behav.* 2013;17:168–73.
51. Zhang Y, et al. The impact of substance use on adherence to antiretroviral therapy among HIV-infected women in the United States. *AIDS Behav.* 2018;22:896–908.
  52. Parsons JT, Starks TJ, Millar BM, Boonrai K, Marcotte D. Patterns of substance use among HIV-positive adults over 50: implications for treatment and medication adherence. *Drug Alcohol Depend.* 2014;139:33–40.
  53. Funke B, et al. High prevalence of recreational and illicit drug use in German people living with HIV with a potential for drug–drug interactions with antiretroviral therapy. *Int J STD AIDS.* 2020;32:75–82.
  54. McCance-Katz EF. Drug interactions associated with methadone, buprenorphine, cocaine, and HIV medications: Implications for pregnant women. *Life Sci.* 2011;88:953–8.
  55. Mora LDL, et al. Do ART and chemsex drugs get along? potential drug–drug interactions in a cohort of people living with HIV who engaged in chemsex: a retrospective observational study. *Infect Dis Ther.* 2022;11:2111–24.
  56. Marzolini C, et al. Prevalence of comedications and effect of potential drug–drug interactions in the Swiss HIV cohort study. *Antivir Ther.* 2010;15:413–23.
  57. Nacheha JB, Hsu AJ, Uthman OA, Spinewine A, Pham PA. Antiretroviral therapy adherence and drug–drug interactions in the aging HIV population. *AIDS.* 2012;26:S39–53.
  58. Nijhawan A, Kim S, Rich JD. Management of HIV infection in patients with substance use problems. *Curr Infect Dis Rep.* 2008;10:432.
  59. Altice FL, Kamarulzaman A, Soriano VV, Schechter M, Friedland GH. Treatment of medical, psychiatric, and substance-use comorbidities in people infected with HIV who use drugs. *Lancet.* 2010;376:367–87.
  60. Monnig MA, et al. Associations of alcohol use, HIV infection, and age with brain white matter microstructure. *J NeuroVirol.* 2021;27:936–50.
  61. Chilunda V, Calderon TM, Martinez-Aguado P, Berman JW. The impact of substance abuse on HIV-mediated neuropathogenesis in the current ART era. *Brain Res.* 2019;1724:146426.
  62. Angeles CPL, los, et al. Lower total and regional grey matter brain volumes in youth with perinatally-acquired HIV infection: associations with HIV disease severity, substance use, and cognition. *Brain Behav Immun.* 2017;62:100–9.
  63. O'Connor E, Zeffiro T. Is treated HIV infection still toxic to the brain? *Prog Mol Biol Transl Sci.* 2019;165:259–84.
  64. Byrd DA, et al. Neurocognitive impact of substance use in HIV Infection. *JAIDS J Acquir Immune Defic Syndr.* 2011;58:154–62.
  65. Chibanda D, Benjamin L, Weiss HA, Abas M. Mental, neurological, and substance use disorders in people living with HIV and sol; AIDS in low- and middle-income countries. *JAIDS J Acquir Immune Defic Syndr.* 2014;67:554–67.
  66. Pimentel E, Sivalingam K, Doke M, Samikkannu T. Effects of drugs of abuse on the blood-brain barrier: a brief overview. *Front Neurosci-switz.* 2020;14:513.
  67. Dash S, Balasubramaniam M, Viallata F, Dash C, Pandhare J. Impact of cocaine abuse on HIV pathogenesis. *Front Microbiol.* 2015;6:1111.
  68. Willson TM, Kliever SA. Pxr, car and drug metabolism. *Nat Rev Drug Discov.* 2002;1:259–66.
  69. Xu C, Li CY-T, Kong A-NT. Induction of phase I, II and III drug metabolism/transport by xenobiotics. *Arch Pharmacol Res.* 2005;28:249–68.
  70. Tolson AH, Wang H. Regulation of drug-metabolizing enzymes by xenobiotic receptors: PXR and CAR. *Adv Drug Deliv Rev.* 2010;62:1238–49.
  71. Moscovitz JE, et al. Establishing transcriptional signatures to differentiate PXR- CAR- and AhR-mediated regulation of drug metabolism and transport genes in cryopreserved human hepatocytes. *J Pharmacol Exp Ther.* 2018. <https://doi.org/10.1124/jpet.117.247296>.
  72. Chen Y, et al. Nuclear receptors in the multidrug resistance through the regulation of drug-metabolizing enzymes and drug transporters. *Biochem Pharmacol.* 2012;83:1112–26.
  73. Prakash C. et al. Nuclear Receptors in Drug Metabolism, Drug Response and Drug Interactions. *Nucl. Recept. Res.* 2015;2.
  74. Chai X, Zeng S, Xie W. Nuclear receptors PXR and CAR: implications for drug metabolism regulation, pharmacogenomics and beyond. *Expert Opin Drug Metab Toxicol.* 2013;9:253–66.
  75. Lemmen J, Tozakidis IEP, Bele P, Galla H-J. Constitutive androstane receptor upregulates Abcb1 and Abcg2 at the blood–brain barrier after CITCO activation. *Brain Res.* 2013;1501:68–80.
  76. Chan GNY, Hoque MdT, Cummins CL, Bendayan R. Regulation of P-glycoprotein by orphan nuclear receptors in human brain microvessel endothelial cells. *J Neurochem.* 2011;118:163–75.
  77. Dauchy S, et al. ABC transporters, cytochromes P450 and their main transcription factors: expression at the human blood–brain barrier. *J Neurochem.* 2008;107:1518–28.
  78. Wang X, Sykes DB, Miller DS. Constitutive androstane receptor-mediated up-regulation of ATP-driven xenobiotic efflux transporters at the blood-brain barrier. *Mol Pharmacol.* 2010;78:376–83.
  79. Miller D. Regulation of ABC transporters at the blood–brain barrier. *Clin Pharmacol Ther.* 2015;97:395–403.
  80. Declèves X, et al. Interplay of drug metabolizing CYP450 Enzymes and ABC transporters in the blood-brain barrier. *Curr Drug Metab.* 2011;12:732–41.
  81. Ott M, Fricker G, Bauer B. Pregnane X receptor (PXR) regulates p-glycoprotein at the blood-brain barrier: functional similarities between Pig and Human PXR. *J Pharmacol Exp Ther.* 2009;329:141–9.
  82. Eng ME, Imperio GE, Bloise E, Matthews SG. ATP-binding cassette (ABC) drug transporters in the developing blood–brain barrier: role in fetal brain protection. *Cell Mol Life Sci.* 2022;79:415.
  83. Gong Y, et al. Pharmacokinetics and pharmacodynamics of cytochrome P450 inhibitors for HIV treatment. *Expert Opin Drug Met.* 2019;15:417–27.
  84. Desai N, et al. An update on drug–drug interactions between antiretroviral therapies and drugs of abuse in HIV systems. *Expert Opin Drug Metab Toxicol.* 2020;16:1005–18.
  85. Eugenin EA, et al. CCL2/Monocyte chemoattractant protein-1 mediates enhanced transmigration of human immunodeficiency virus (HIV)-infected leukocytes across the blood-brain barrier: a potential mechanism of HIV–CNS invasion and NeuroAIDS. *J Neurosci.* 2006;26:1098–106.
  86. Williams DW, et al. CCR2 on CD14(+)/CD16(+) monocytes is a biomarker of HIV-associated neurocognitive disorders. *Neurol Neuroimmunol Neuroinflammation.* 2014;1:e36.
  87. Eugenin EA, Berman JW. Chemokine-dependent mechanisms of leukocyte trafficking across a model of the blood–brain barrier. *Methods.* 2003;29:351–61.
  88. Weiss JM, Nath A, Major EO, Berman JW. HIV-1 tat induces monocyte chemoattractant protein-1-mediated monocyte transmigration across a model of the human blood-brain barrier and up-regulates CCR5 expression on human monocytes. *J Immunol.* 1999;163:2953–9.
  89. Williams DW, Anastos K, Morgello S, Berman JW. JAM-A and ALCAM are therapeutic targets to inhibit diapedesis across the BBB of CD14+CD16+ monocytes in HIV-infected individuals. *J Leukocyte Biol.* 2014;97:401–12.
  90. Williams DW, et al. Mechanisms of HIV entry into the CNS: increased sensitivity of HIV infected CD14+CD16+ monocytes to CCL2 and key roles of CCR2, JAM-A, and ALCAM in diapedesis. *PLoS ONE.* 2013;8:e69270.
  91. Williams DW, Tesfa L, Berman JW. Novel flow cytometric analysis of the blood-brain barrier. *Cytom Part J Int Soc Anal Cytol.* 2015;87:897–907.
  92. Dooley KE, et al. Once-weekly rifampine and isoniazid for tuberculosis prevention in patients with HIV taking dolutegravir-based antiretroviral therapy: a phase 1/2 trial. *Lancet HIV.* 2020;7:e401–9.
  93. McGowan IM, et al. An open-label pharmacokinetic and pharmacodynamic assessment of tenofovir gel and oral Emtricitabine/Tenofovir Disoproxil Fumarate. *AIDS Res Hum Retroviruses.* 2022;38:279–87.
  94. DiFrancesco R, et al. Clinical pharmacology quality assurance program. *Ther Drug Monit.* 2013;35:631–42.
  95. (CVM), U. S. D. of H. and H. S., Food and Drug Administration, Center for Drug Evaluation and Research (CDER), Center for Veterinary Medicine. Bioanalytical Method Validation. *Biopharmaceutics.* 2018. <https://www.fda.gov/files/drugs/published/Bioanalytical-Method-Validation-Guidance-for-Industry.pdf>.
  96. Blaho K, Logan B, Winbery S, Park L, Schwilke E. Blood cocaine and metabolite concentrations, clinical findings, and outcome of patients presenting to an ED. *Am J Emerg Med.* 2000;18:593–8.

97. Wiśniewski JR, Hein MY, Cox J, Mann M. A "proteomic ruler" for protein copy number and concentration estimation without spike-in standards\*. *Mol Cell Proteom.* 2014;13:3497–506.
98. Müller H, et al. New functional assay of P-glycoprotein activity using Hoechst 33342. *Bioorg Med Chem.* 2007;15:7470–9.
99. Tang F, Ouyang H, Yang JZ, Borchardt RT. Bidirectional transport of rhodamine 123 and Hoechst 33342, fluorescence probes of the binding sites on P-glycoprotein, across MDCK–MDR1 cell monolayers. *J Pharm Sci.* 2004;93:1185–94.
100. Srinivas N, et al. Antiretroviral concentrations and surrogate measures of efficacy in the brain tissue and CSF of preclinical species. *Xenobiotica.* 2019;49:1–35.
101. Ferrara M, et al. Antiretroviral drug concentrations in brain tissue of adult decedents. *Aids Lond Engl.* 2020. <https://doi.org/10.1097/QAD.0000000000002628>.
102. Devanathan AS, et al. Antiretroviral penetration across three preclinical animal models and humans in eight putative HIV viral reservoirs. *Antimicrob Agents.* 2019. <https://doi.org/10.1128/AAC.01639-19>.
103. Patel SH, et al. Cell-type specific differences in antiretroviral penetration and the effects of HIV-1 Tat and morphine among primary human brain endothelial cells, astrocytes, pericytes, and microglia. *Neurosci Lett.* 2019;712:134475.
104. Lanman T, Letendre S, Ma Q, Bang A, Ellis R. CNS neurotoxicity of antiretrovirals. *J Neuroimmune Pharm.* 2021;16:130–43.
105. Zhang D, et al. Drug concentration asymmetry in tissues and plasma for small molecule-related therapeutic modalities. *Drug Metab Dispos.* 2019;47:1122–35.
106. Dash PK, Akay-Espinoza C. FDG PET/computed tomography can detect region-specific neuronal changes following antiretroviral therapy in HIV-infected patients. *AIDS.* 2021;35:1309–10.
107. Sonti S, Sharma AL, Tyagi M. HIV-1 Persistence in the CNS: mechanisms of latency, pathogenesis and an update on eradication strategies. *Virus Res.* 2021;303:198523.
108. Dyavar SR, et al. Intramuscular and subcutaneous administration of antiretroviral drugs, compared with oral, enhances delivery to lymphoid tissues in BALB/c mice. *J Antimicrob Chemother.* 2021. <https://doi.org/10.1093/jac/dkab228>.
109. Srinivas N, et al. Predicting efavirenz concentrations in the brain tissue of HIV-infected individuals and exploring their relationship to neurocognitive impairment. *Clin Transl Sci.* 2019;12:302–11.
110. Patel SH, et al. Simultaneous determination of intracellular concentrations of tenofovir, emtricitabine, and dolutegravir in human brain microvascular endothelial cells using liquid chromatography–tandem mass spectrometry (LC–MS/MS). *Anal Chim Acta.* 2019;1056:79–87.
111. Osborne O, Peyravian N, Nair M, Daunert S, Toborek M. The paradox of HIV blood-brain barrier penetrance and antiretroviral drug delivery deficiencies. *Trends Neurosci.* 2020;43:695–708.
112. Williams DW, Eugenin EA, Calderon TM, Berman JW. Monocyte maturation, HIV susceptibility, and transmigration across the blood brain barrier are critical in HIV neuropathogenesis. *J Leukocyte Biol.* 2012;91:401–15.
113. Wiriyakosol N, et al. A LC/MS/MS method for determination of tenofovir in human plasma and its application to toxicity monitoring. *J Chromatogr B.* 2018;1085:89–95.
114. Bennetto-Hood C, Tabolt G, Savina P, Acosta EP. A sensitive HPLC–MS/MS method for the determination of dolutegravir in human plasma. *J Chromatogr B.* 2014;945:225–32.
115. Matta M, Pilli N, J.V.L.N., S. R. A validated liquid chromatography and tandem mass spectrometric method for simultaneous quantitation of tenofovir, emtricitabine, and efavirenz in human plasma and its pharmacokinetic application. *Acta Chromatogr.* 2015;27:27–39.
116. Gish RG, et al. Dose range study of pharmacokinetics, safety, and preliminary antiviral activity of emtricitabine in adults with hepatitis B virus infection. *Antimicrob Agents Chemother.* 2002;46:1734–40.
117. Molina J, et al. Pharmacokinetics of emtricitabine, didanosine and efavirenz administered once-daily for the treatment of HIV-infected adults (pharmacokinetic substudy of the ANRS 091 trial)\*. *Hiv Med.* 2004;5:99–104.
118. Dumond J, et al. Pharmacokinetics of two common antiretroviral regimens in older HIV-infected patients: a pilot study. *Hiv Med.* 2013;14:401–9.
119. Delahunty T, Bushman L, Fletcher CV. Sensitive assay for determining plasma tenofovir concentrations by LC/MS/MS. *J Chromatogr B.* 2006;830:6–12.
120. Zhao L, et al. Simultaneous determination of tenofovir alafenamide and tenofovir in human plasma by LC–MS/MS and its application to pharmacokinetics study in clinic. *J Chromatogr B.* 2019;1117:148–57.
121. Peng X, Luo Z, He S, Zhang L, Li Y. Blood-brain barrier disruption by lipopolysaccharide and sepsis-associated encephalopathy. *Front Cell Infect Microbiol.* 2021;11:768108.
122. Nishioku T, et al. Detachment of brain pericytes from the basal lamina is involved in disruption of the blood-brain barrier caused by lipopolysaccharide-induced sepsis in mice. *Cell Mol Neurobiol.* 2009;29:309–16.
123. Xao H, Banks WA, Niehoff ML, Morley JE. Effect of LPS on the permeability of the blood–brain barrier to insulin. *Brain Res.* 2001;896:36–42.
124. Jaeger LB, et al. Lipopolysaccharide alters the blood–brain barrier transport of amyloid  $\beta$  protein: a mechanism for inflammation in the progression of Alzheimer's disease. *Brain Behav Immun.* 2009;23:507–17.
125. Barton, S. M. et al. Lipopolysaccharide Induced Opening of the Blood Brain Barrier on Aging 5XFAD Mouse Model. *J Alzheimer's Dis.* 2019; 67(2):503–13. <https://doi.org/10.3233/JAD-180755>.
126. Sumi N, et al. Lipopolysaccharide-activated microglia induce dysfunction of the blood-brain barrier in rat microvascular endothelial cells co-cultured with microglia. *Cell Mol Neurobiol.* 2010;30:247–53.
127. Banks WA, et al. Lipopolysaccharide-induced blood-brain barrier disruption: roles of cyclooxygenase, oxidative stress, neuroinflammation, and elements of the neurovascular unit. *J Neuroinflammation.* 2015;12:223.
128. Gaillard PJ, de Boer AB, Breimer DD. Pharmacological investigations on lipopolysaccharide-induced permeability changes in the blood–brain barrier in vitro. *Microvasc Res.* 2003;65:24–31.
129. Hartz AMS, Bauer B, Fricker G, Miller DS. Rapid modulation of P-glycoprotein-mediated transport at the blood-brain barrier by tumor necrosis factor- $\alpha$  and lipopolysaccharide. *Mol Pharmacol.* 2006;69:462–70.
130. Castellino S, et al. Metabolism, excretion, and mass balance of the HIV-1 integrase inhibitor dolutegravir in humans. *Antimicrob Agents Ch.* 2013;57:3536–46.
131. Renwick AB, Surry D, Price RJ, Lake BG, Evans DC. Metabolism of 7-benzyloxy-4-trifluoromethylcoumarin by human hepatic cytochrome P450 isoforms. *Xenobiotica.* 2008;30:955–69.
132. Sevrioukova IF, Poulos TL. Monooxygenase, peroxidase and peroxxygenase properties and mechanisms of cytochrome P450. *Adv Exp Med Biol.* 2015;851:83–105.
133. Manda VK, et al. PXR mediated induction of CYP3A4, CYP1A2, and P-gp by *Mitragyna speciosa* and its alkaloids. *Phytother Res.* 2017;31:1935–45.
134. Sacktor N, et al. CSF antiretroviral drug penetrance and the treatment of HIV-associated psychomotor slowing. *Neurology.* 2001;57:542–4.
135. Evers S, et al. Prevention of AIDS dementia by HAART does not depend on cerebrospinal fluid drug penetrance. *AIDS Res Hum Retroviruses.* 2004;20:483–91.
136. Letendre S, et al. Validation of the CNS penetration–effectiveness rank for quantifying antiretroviral penetration into the central nervous system. *Arch Neurol.* 2008;65:65–70.
137. Mdanda S, et al. Investigating time dependent brain distribution of nevirapine via mass spectrometric imaging. *J Mol Histol.* 2019;50:593–9.
138. Ntshangase S, et al. Spatial distribution of elvitegravir and tenofovir in rat brain tissue: application of matrix-assisted laser desorption/ionization mass spectrometry imaging and liquid chromatography/tandem mass spectrometry. *Rapid Commun Mass Spectrom.* 2019;33:1643–51.
139. Seneviratne HK, Hamlin AN, Heck CJS, Bumpus NN. Spatial distribution profiles of emtricitabine, tenofovir, efavirenz, and rilpivirine in murine tissues following in vivo dosing correlate with their safety profiles in humans. *ACS Pharmacol Transl Sci.* 2020;3:655–65.
140. Chang L, Ernst T, Speck O, Grob CS. Additive effects of HIV and chronic methamphetamine use on brain metabolite abnormalities. *Am J Psychiatry.* 2005;162:361–9.
141. Martin EM, Gonzalez R, Vassileva J, Bechara A. Double dissociation of HIV and substance use disorder effects on neurocognitive tasks dependent on striatal integrity. *AIDS.* 2019;33:1863–70.
142. Rosenbloom MJ, Sullivan EV, Pfefferbaum A. Focus on the brain: HIV infection and alcoholism: comorbidity effects on brain structure and function. *Alcohol Res Heal.* 2010;33:247–57.

143. Saloner R, et al. Methamphetamine and cannabis: a tale of two drugs and their effects on HIV, brain, and behavior. *J Neuroimmune Pharmacol*. 2020;15:743–64.
144. Murdoch DM, et al. Neuroimaging and immunological features of neurocognitive function related to substance use in people with HIV. *J NeuroVirol*. 2023;29:78–93.
145. Group, T. T., et al. Substance use is a risk factor for neurocognitive deficits and neuropsychiatric distress in acute and early HIV infection. *J NeuroVirol*. 2013;19:65–74.
146. Siqueira M, Stipursky J. Blood brain barrier as an interface for alcohol induced neurotoxicity during development. *Neurotoxicology*. 2022;90:145–57.
147. Yao H, et al. Cocaine hijacks  $\alpha 1$  receptor to initiate induction of activated leukocyte cell adhesion molecule: implication for increased monocyte adhesion and migration in the CNS. *J Neurosci Official J Soc Neurosci*. 2011;31:5942–55.
148. Davidson TL, et al. Cocaine impairs serial-feature negative learning and blood-brain barrier integrity. *Pharmacol Biochem Behav*. 2018;170:56–63.
149. Dhillon NK, et al. Cocaine-mediated alteration in tight junction protein expression and modulation of CCL2/CCR2 axis across the blood-brain barrier: implications for HIV-dementia. *J Neuroimmune Pharm*. 2008;3:52–6.
150. Calderon TM, et al. Dopamine increases CD14+CD16+ monocyte transmigration across the blood brain barrier: implications for substance abuse and HIV neuropathogenesis. *J Neuroimmune Pharm*. 2017;12:353–70.
151. Sajja RK, Rahman S, Cucullo L. Drugs of abuse and blood-brain barrier endothelial dysfunction: a focus on the role of oxidative stress. *J Cereb Blood Flow Metab*. 2015;36:539–54.
152. Patel S, et al. Effects of HIV-1 tat and methamphetamine on blood-brain barrier integrity and function in vitro. *Antimicrob Agents Chemother*. 2017. <https://doi.org/10.1128/AAC.01307-17>.
153. Bhalerao A, Cucullo L. HIV-1 gp120 and tobacco smoke synergistically disrupt the integrity of the blood-brain barrier. *Eur J Cell Biol*. 2022;101: 151271.
154. Liao K, Niu F, Hu G, Buch S. Morphine-mediated release of astrocyte-derived extracellular vesicle miR-23a induces loss of pericyte coverage at the blood-brain barrier: Implications for neuroinflammation. *Front Cell Dev Biol*. 2022;10:984375.
155. Pang L, Wang Y. Overview of blood-brain barrier dysfunction in methamphetamine abuse. *Biomed Pharmacother*. 2023;161:114478.
156. Fattakhov N, Torices S, Stangis M, Park M, Toborek M. Synergistic impairment of the neurovascular unit by HIV-1 infection and methamphetamine use: implications for HIV-1-associated neurocognitive disorders. *Viruses*. 2021;13:1883.
157. Kousik SM, Napier TC, Carvey PM. The Effects of psychostimulant drugs on blood brain barrier function and neuroinflammation. *Front Pharmacol*. 2012;3:121.
158. Mayer KH, et al. Emtricitabine and tenofovir alafenamide vs emtricitabine and tenofovir disoproxil fumarate for HIV pre-exposure prophylaxis (DISCOVER): primary results from a randomised, double-blind, multicentre, active-controlled, phase 3, non-inferiority trial. *Lancet*. 2020;396:239–54.
159. Riddell J, Amico KR, Mayer KH. HIV preexposure prophylaxis: a review. *JAMA*. 2018;319:1261–8.
160. Desai M, Field N, Grant R, McCormack S. Recent advances in pre-exposure prophylaxis for HIV. *BMJ*. 2017;359:j5011.
161. Thomson KA, et al. Tenofovir-based oral preexposure prophylaxis prevents HIV infection among women. *Curr Opin HIV AIDS*. 2016;11:18–26.
162. Kadry H, Noorani B, Cucullo L. A blood-brain barrier overview on structure, function, impairment, and biomarkers of integrity. *Fluids Barriers CNS*. 2020;17:69.
163. Pardridge WM. Drug transport across the blood-brain barrier. *J Cereb Blood Flow Metabolism*. 2012;32:1959–72.
164. Neuwelt E, et al. Strategies to advance translational research into brain barriers. *Lancet Neurol*. 2008;7:84–96.
165. Pardridge WM. The blood-brain barrier: Bottleneck in brain drug development. *NeuroRx*. 2005;2:3–14.
166. Wu D, et al. The blood-brain barrier: structure, regulation, and drug delivery. *Signal Transduct Target Ther*. 2023;8:217.
167. Carroll FI, Lewin AH, Boja JW, Kuhar MJ. Cocaine receptor: biochemical characterization and structure-activity relationships of cocaine analogs at the dopamine transporter. *J Med Chem*. 1992;35:969–81.
168. Ritz MC, Lamb RJ, Goldberg SR, Kuhar MJ. Cocaine receptors on dopamine transporters are related to self-administration of cocaine. *Science*. 1987;237:1219–23.
169. Volkow ND, et al. Relationship between subjective effects of cocaine and dopamine transporter occupancy. *Nature*. 1997;386:827–30.
170. Beuming T, et al. The binding sites for cocaine and dopamine in the dopamine transporter overlap. *Nat Neurosci*. 2008;11:780–9.
171. Hall FS, et al. Cocaine-conditioned locomotion in dopamine transporter, norepinephrine transporter and 5-HT transporter knockout mice. *Neuroscience*. 2009;162:870–80.
172. Schroeter S, et al. Immunolocalization of the cocaine- and antidepressant-sensitive I-norepinephrine transporter. *J Comp Neurol*. 2000;420:211–32.
173. Zhu MY, Shamburger S, Li J, Ordway GA. Regulation of the human norepinephrine transporter by cocaine and amphetamine. *J Pharmacol Exp Ther*. 2000;295:951–9.
174. Ramamoorthy S, et al. Antidepressant—and cocaine-sensitive human serotonin transporter: molecular cloning, expression, and chromosomal localization. *Proc Natl Acad Sci*. 1993;90:2542–6.
175. Ritz MC, Cone EJ, Kuhar MJ. Cocaine inhibition of ligand binding at dopamine, norepinephrine and serotonin transporters: A structure-activity study. *Life Sci*. 1990;46:635–45.
176. Sora I, et al. Cocaine reward models: Conditioned place preference can be established in dopamine- and in serotonin-transporter knockout mice. *Proc Natl Acad Sci*. 1998;95:7699–704.
177. Sora I, et al. Molecular mechanisms of cocaine reward: combined dopamine and serotonin transporter knockouts eliminate cocaine place preference. *Proc Natl Acad Sci*. 2001;98:5300–5.
178. Hall FS, et al. Molecular mechanisms underlying the rewarding effects of cocaine. *Ann N York Acad Sci*. 2004;1025:47–56.
179. Chen J-G, Sachpatzidis A, Rudnick G. The third transmembrane domain of the serotonin transporter contains residues associated with substrate and cocaine binding\*. *J Biol Chem*. 1997;272:28321–7.
180. Chen W, et al. Cocaine-induced structural and functional impairments of the glymphatic pathway in mice. *Brain Behav Immun*. 2020;88:97–104.
181. Clauss NJ, et al. Ethanol inhibits dopamine uptake via organic cation transporter 3: Implications for ethanol and cocaine co-abuse. *Mol Psychiatry*. 2023. <https://doi.org/10.1038/s41380-023-02064-5>.
182. Manyanga J, et al. Electronic cigarette aerosols alter the expression of cisplatin transporters and increase drug resistance in oral cancer cells. *Sci Rep*. 2021;11:1821.
183. Kumar S, Earla R, Jin M, Mitra AK, Kumar A. Effect of ethanol on spectral binding, inhibition, and activity of CYP3A4 with an antiretroviral drug nelfinavir. *Biochem Biophys Res Commun*. 2010;402:163–7.
184. Jin M, et al. Effect of alcohol on drug efflux protein and drug metabolic enzymes in U937 macrophages. *Alcohol Clin Exp Res*. 2011;35:132–9.
185. Tega Y, Yamazaki Y, Akanuma S, Kubo Y, Hosoya K. Impact of Nicotine transport across the blood-brain barrier: carrier-mediated transport of nicotine and interaction with central nervous system drugs. *Biol Pharm Bull*. 2018;41:1330–6.
186. Wong LT, Smyth DD, Sitar DS. Interference with renal organic cation transport by (-) and (+)-nicotine at concentrations documented in plasma of habitual tobacco smokers. *J Pharmacol Exp Ther*. 1992;261:21–5.
187. Chaves C, Remião F, Cisternino S, Declèves X. Opioids and the blood-brain barrier: a dynamic interaction with consequences on drug disposition in brain. *Curr Neuropharmacol*. 2017;15:1156–73.
188. Ladak F, et al. Substance use Patterns and HIV-1 RNA Viral Load Rebound among HIV-Positive Illicit Drug users in a Canadian Setting. *Antivir Ther*. 2018;24:19–25.
189. Liang J, et al. Longitudinal patterns of illicit drug use, antiretroviral therapy exposure and plasma HIV-1 RNA viral load among HIV-positive people who use illicit drugs. *AIDS*. 2020;34:1389–96.
190. Stover S, Milloy M-J, Grant C, Fairbairn N, Socias ME. Estimating the minimum antiretroviral adherence required for plasma HIV-1 RNA viral load suppression among people living with HIV who use unregulated drugs. *AIDS*. 2022;36:1233–43.
191. Deutsch EW, et al. The ProteomeXchange consortium at 10 years: 2023 update. *Nucleic Acids Res*. 2022;51:D1539–48.

## Publisher's Note

Springer Nature remains neutral with regard to jurisdictional claims in published maps and institutional affiliations.